Taylor & Francis
Taylor & Francis Group

Check for updates

On subsurface multiple inclusions model under transient *SH*-wave propagation

Saeed Mojtabazadeh-Hasanlouei [a], Mehdi Panji [a] and Mohsen Kamalian [b]

aDepartment of Civil Engineering, Zanjan Branch, Islamic Azad University, Zanjan, Iran; bGeotechnical Engineering Research Center, International Institute of Earthquake Engineering and Seismology, Tehran, Iran

ABSTRACT

In this paper, a homogeneous linear elastic half-plane model cluttered with multiple embedded arbitrarily-shaped inclusions is presented. The model was built based on the time-domain boundary element method established via the half-space Green's functions, subjected to propagating obliquely incident SH-waves. Using this method, the discretization was performed only on the interfaces. The full-contact posture was assumed between the inclusions and the surrounding domain. First, the problem was disintegrated into two parts including a multi-pitted half-plane and a system of randomly shaped closed filled solids. Then, by applying the method to each part, the influence coefficients of the matrices were obtained. Finally, to form a coupled equation for determining unknown boundary values in each time-step, the boundary/continuity conditions were satisfied on the interfaces. By implementing the method in an advanced developed algorithm, its efficiency was investigated by comparing the responses with those of the published works. To complete the obtained results, the synthetic seismograms and three-dimensional amplification patterns of the surface were presented. Also, some snapshots were illustrated to reveal the dispersion of the waves. The proposed method is a powerful tool for modeling various structures at the nano-scale and can be recommended to engineers for transient analysis of composite materials.

CONTACT Mehdi Panji ✉ m.panji@iauz.ac.ir
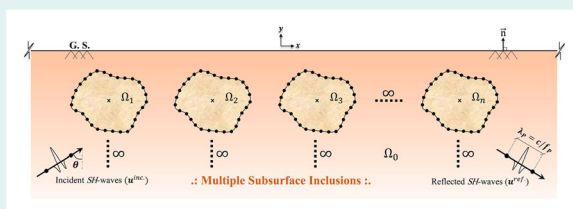
1. Introduction

In the last decades, recognition of seismic ground motions and damage investigations in the presence of subsurface heterogeneities during an earthquake has been among the most important concerns of seismologists. This issue is more significant for subsurface inclusions because of their dissimilar materials to the surrounding medium. This feature can change the initial nature of incidence waves by diffraction, reflection, crawling, diversion, and trapping, leading to amplification/de-amplification on different zones of the surface. Therefore, evaluation of various effective factors such as geometry and type of features, site conditions, type of incident waves, and paths of wave motion requires using appropriate approaches for their analysis and detailed understanding. Utilizing these methods allows modeling and analyzing the problems of wave scattering and predicting the real responses in seismic mode. Technically, researchers have proposed various approaches for seismic analysis. Overall, these methods can be divided into analytical, semi-analytical, experimental, and numerical methods [1]. In the use of analytical and semi-analytical approaches for inclusion problems, the pioneering studies were done in the late 1970s. For instance, Simons [2] addressed the scattering of *SH*-waves by semi-infinite inclusions using an exponential expansion method. Kikuchi [3, 4] developed the model of uniformly distributed inclusions using the wave function expansion method. Later, Coussy [5] presented a study about the scattering of elastic *P* and *SV*-waves by inclusion with an interface crack and extracted the closed-form solution for this problem. The scattering of elastic *SH*-waves in the presence of a rigid cylindrical inclusion was studied by Wang & Wang [6]. In the following years, using the wave function expansion method, Zhao & Qi [7] investigated the scattering of plane *SH*-wave in the presence of a shallow cylindrical elastic inclusion. A year after, based on the multiple wave propagation theory, Conoir & Norris [8] modeled and analyzed an elastic medium containing random configurations of cylindrical scatterers. Using the multipole method, Lee & Chen [9] analytically solved the scattering of the flexural wave by multiple circular inclusions in an infinite thin plate. Recently, Qi et al. [10] utilized wave function expansion method to study the dynamic response of a plate with multiple inclusions subjected to *SH*-waves. Despite the high accuracy of analytical methods, their lack of flexibility in modeling and analysis of complex and multiple features has forced the researchers to use alternative approaches such as numerical methods.

In recent years, increasing the power and capacity of computers and their advanced components has facilitated solving complex engineering problems using numerical methods [11]. When using numerical methods, one can never claim that the obtained results are completely exact; rather, the main purpose is to move toward accurate responses as close as possible. The numerical methods are divided into two general categories known as the domain and boundary methods. The common domain methods include the finite element method (FEM) and finite difference method (FDM). Among the pioneering studies on FEM are those of Lysmer & Drake [12], Smith [13], Day [14] and Kawase & Sato [15], who highlighted the application of this approach for analysis of wave propagation problems in seismology. Zhang & Katsube [16] presented a hybrid FEM for the analysis of heterogeneous materials with randomly-dispersed elastic inclusions. Using a FEM-based numerical equivalent inclusion method, Nakasone et al. [17] analyzed the stress fields in and around the various shapes of inclusions. In the use of FDM, Boore [18], Ohtsuki & Harumi [19] and Moczo & Bard [20] are the pioneering researchers who studied the effects

of topography and subsurface inhomogeneities on the wave diffraction and amplification of the surface subjected to seismic *SH-* and *SV*-waves. The boundary methods are separated into two categories including full-plane and half-plane, each being developed in transformed (frequency and Laplace) and time domains as well [21]. Using the boundary element method (BEM), one dimension of the models is reduced and the radiation conditions of waves at infinity are satisfied. The advantages of using BEM compared to the domain approaches include concentration of meshes only around the boundary of desired topographic features (the target society of this study includes subsurface inclusions), automatic satisfaction of wave radiation conditions in far boundaries, lower volume of input data, lower memory seizure, significant reduction in analysis time, and extremely high accuracy of exported results because of the large contribution of analytical processes in solving problems [22].

In full-plane BEM, the model should be truncated from a full-space and the boundaries should be closed in a distance far away from the desired zone. This leads to the approximate satisfaction of stress-free conditions on the ground surface [23]. Panji et al. [24] and Panji et al. [25] used the static full-plane BEM to evaluate the effective parameters on the stability of underground tunnels. Using dynamic full-plane BEM, Hadley [26] studied the wave propagation by inclusions embedded in a nonhomogeneous elastic half-space. Using a 2D hybrid FE/BE method, Kamalian et al. [27] presented the site response analysis of non-homogeneous features in time-domain. Parvanova et al. [28] investigated the dynamic responses of a medium with multiple inclusions under anti-plane strain conditions. Later, Parvanova et al. [29] focused on the wave scattering in the presence of nano-heterogeneities embedded in an elastic matrix. In another study by BE/FE method, Parvanova et al. [30] focused on the dynamic analysis of nano-heterogeneities located in a finite-sized medium. In the half-plane BEM approach, the stress-free boundary condition of the ground surface is satisfying in an exact process. Despite difficult implementation and creating bulky equations in the half-plane BEM compared to the full-plane BEM, there is no need to discretize the smooth surface and define fictitious elements for enclosing boundaries. These advantages help to make the models simpler. Using static half-plane BEM, Panji et al. [31] and Panji & Ansari [32] analyzed shallow tunnels and pressure pipes embedded in layered soils, respectively. In a dynamic study by half-plane BEM, Dong et al. [33] studied the seismic behavior of subsurface features such as pipes and inclusions.

Among the pioneering studies by transformed-domain BEM is the work of Dravinski [34], who determined the ground motion amplification due to elastic inclusion located in a half-space. Then, Niwa & Hirose [35] presented the application of the boundary integral equation (BIE) method for transient analysis of inclusions in half-space. Next, Hadley et al. [36] studied the scattering of seismic waves due to inclusions in a nonhomogeneous elastic half-space. Using an indirect BIE approach, Benites et al. [37, 38] and Yomogida et al. [39] investigated antiplane/plane strain elastic wave scattering for a system of multiple cavities. The models were presented in full space and half-space subjected to the plane *SH*, *P*, and *SV*-waves. Yao et al. [40] simulated the 2D behavior of randomly distributed inclusions as a composite materials problem. Rus & Gallego [41] presented a boundary integral equation for sensitivity analysis of inclusion and cavity features in the harmonic elastodynamic medium. Mogilevskaya et al. [42] studied the multiple interacting of circular nano-inhomogeneities. Based on the double-layer potentials, Chen et al. [43] presented a meshless method for antiplane shear problems with multiple inclusions. The scattering of plane harmonic *SH*, *P*,

SV, and *Rayleigh*-waves by a completely embedded corrugated elastic inclusion was presented by Yu & Dravinski [44, 45] investigated the scattering of plane harmonic *SH*-waves in the presence of multiple subsurface inclusions. Using the BIE method, Parvanova et al. [46] investigated the scattering of seismic waves by nano-heterogeneities embedded in an elastic matrix. In the same year, the scattering of a plane harmonic *SH*-wave by a rough multilayered inclusion of arbitrary shape was obtained by Dravinski & Sheikhhassani [47]. The effect of position and shape of inclusions in a conductor domain was addressed by Peters & Barra [48]. In the studies of Lee & Chen [49] and Chen et al. [50], a null-field BIE method presented for analyzing the antiplane problems with elliptical inclusions to obtain the scattering of the *SH*-wave. Sheikhhassani & Dravinski [51] studied the scattering of a plane harmonic *SH*-wave and by multiple multilayered inclusions located in an elastic half-space subjected to *SH*-waves. In another study, Sheikhhassani & Dravinski [52] focused on the dynamic stress concentration by multiple multilayered inclusions. Utilizing multidomain IBEM, Ba & Yin [53] studied the wave scattering by inclusions in a layered half-space. Recently, Jobin et al. [54] evaluated the interaction between inclusions using strain intensity factors.

One of the studies by time-domain BEM (TD-BEM) is the one conducted by Feng et al. [55], who presented the 2D scattering of *SH*-waves by inclusion with a unilateral frictional interface. Kamalian et al. [56] obtained the 2D site response of topographic structures. Then, Mykhaskiv [57] presented the transient response of a plane rigid inclusion subjected to the incident wave. Huang et al. [58] suggested a time-domain direct boundary integral method for a viscoelastic plane with circular holes and elastic inclusions. In the following years, Lei et al. [59] analyzed the dynamic crack propagation in a matrix containing inclusions. Panji et al. [22] studied the transient analysis of wave propagation problems. Panji & Ansari [60] presented the *SH*-wave scattering by the lined tunnels located in an elastic half-plane. Panji & Mojtabazadeh-Hasanlouei [61, 62] analyzed the seismic behavior of twin and multiple subsurface cavities and obtained the wave propagation and amplification patterns on the surface. Huang et al. [63] presented the scattering of plane *P* and *SV*-waves by twin lining tunnels with imperfect interfaces embedded in an elastic half-space. In one of the most recent studies, Panji et al. [64] investigated the *SH*-wave dispersion by a single circular and elliptical inclusion and presented time and frequency-domain responses. In another study, Panji & Mojtabazadeh-Hasanlouei [65] presented the transient response of irregular surface by periodically distributed semi-sine shaped valleys subjected to *SH*-waves.

In most previous studies, the models are limited to homogeneous single materials. Also, the time-domain responses for transient analysis of non-homogeneous solids have been obtained by the inverse Fourier/Laplace-transform algorithm from the angle of mechanical problems. In the present study, the multiple scattering of transient *SH*-waves due to an unlimited number of subsurface inclusions is directly analyzed in the time-domain. For this purpose, step-by-step transient analysis of arbitrarily shaped subsurface inclusions is presented subjected to propagating obliquely incident plane *SH*-waves. The models are made up of two separate parts including a multi-pitted half-plane and a system of many alluvial media that are assembled on each other. After implementing the proposed method in the general DASBEM algorithm [22], its validity was evaluated by analyzing several practical examples. Then, as a numerical scheme, the synthetic seismograms and three-dimensional (3D) amplification patterns of the surface were presented for circular/elliptical multiple inclusions. The main objective of the paper is to present the ability and efficiency of the

method in preparation of simple seismic heterogeneous models with different behavior of materials. Moreover, obtaining high accuracy responses, achieving optimal analysis time using a limited number of input data and memory seizure, and combining numerical approaches in a simple way are the most important goals of this study.

2. Problem statement

As shown in Figure 1, a system of arbitrarily shaped infinite inclusions is embedded in a linear elastic homogeneous and isotropic half-plane. In this figure, Ω is the domain and Γ is the boundary of the body, which are defined separately for the pitted domain and the closed filled solids; b is the radius; DR is the depth ratio of inclusions; θ is the angle of the incident waves; and n is the normal vector that is perpendicular to the surface and dependent to the node numbering direction. The models are subjected to the incident out-of-plane SH-waves of the Ricker type [66]. The function of a Ricker wavelet is defined as Equation (1):

$$f(t) = [1 - 2(\pi f_p(t - t_0))^2]e^{-(\pi f_p(t-t_0))^2},$$
(1)

where f_p is the predominant frequency of the wave and t_0 is the time-shifting parameter. Since the modeling is conducted in half-plane and the stress-free boundary conditions are satisfied on the ground surface, free-field displacement (u^{ff}) can be obtained by adding the phase of the incident and reflected waves as follows [67]:

$$u^{ff}(x,y,t) = \alpha_{max} \cdot \left(\begin{array}{l} \left[1 - 2\left(\frac{\pi f_p}{c_0}\alpha^{inc.}\right)^2\right]e^{-\left(\frac{\pi f_p}{c_0}\alpha^{inc.}\right)^2} H\left(t - \frac{r^{inc.}}{c_0}\right) + \\ \left[1 - 2\left(\frac{\pi f_p}{c_0}\alpha^{ref.}\right)^2\right]e^{-\left(\frac{\pi f_p}{c_0}\alpha^{ref.}\right)^2} H\left(t - \frac{r^{ref.}}{c_0}\right) \end{array} \right),$$
(2)

where $\alpha^{inc.}$, $\alpha^{ref.}$, $r^{inc.}$, and $r^{ref.}$ are obtained from Equations (3) and (4):

$$\alpha^{inc.} = c(t - t_0) + r^{inc.}, \quad r^{inc.} = -\sin(\theta) \cdot x + \cos(\theta) \cdot y,$$
(3)

$$\alpha^{ref.} = c(t - t_0) + r^{ref.}, \quad r^{ref.} = -\sin(\theta) \cdot x - \cos(\theta) \cdot y,$$
(4)

To initiate the formulation procedure, the equation of motion for the anti-plane strain model should be utilized as Equation (5):

$$\frac{\partial^2 u(x,y,t)}{\partial x^2} + \frac{\partial^2 u(x,y,t)}{\partial y^2} + b(x,y,t) = \frac{1}{c_j^2}\frac{\partial^2 u(x,y,t)}{\partial t^2}, j = 0, 1, 2, \cdots, n$$
(5)

where $u(x, y, t)$ is out-of-plane displacement and $b(x, y, t)$ is out-of-plane body force at the point (x, y) for the current time of t. The shear-wave velocity of the jth medium is defined by c_j and determined by $\sqrt{\mu_j/\rho_j}$, where μ_j is the shear modulus and ρ_j is the mass density. By solving Equation (5) based on the boundary conditions presented in Equation (6), a 2D
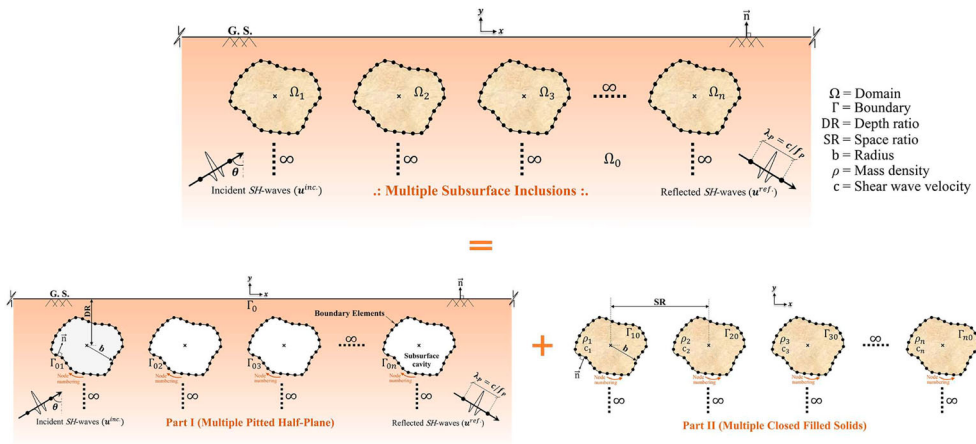
Figure 1. The problem geometry of arbitrarily shaped multiple subsurface inclusions placed in an elastic half-plane subjected to the incident *SH*-waves.

anti-plane semi-infinite medium can be obtained as well.

$$\frac{\partial u(x, y, t)}{\partial n}\bigg|_{y=0} = 0, \tag{6}$$

Moreover, the half-space Green's functions can be achieved by simultaneously taking the singular solution into account for Equations (5) and (6) [22].

3. Half-plane TD-BEM

Using the wave source image technique and satisfying the stress-free boundary conditions on the surface, one can concentrate meshes exclusively around the boundary of inclusions. This procedure significantly simplifies the problem and helps to decrease the volume of input data and time of analysis [22]. The details of this method are mentioned in the following section.

3.1. Boundary integral equation (BIE)

The first step is applying the weighted residual integral on Equation (5) without considering the boundary conditions presented in Equation (6). Then, by twice integration, utilizing boundary methods for eliminating the volumetric integral defined on the domain and ignoring the contributions of the initial conditions and body forces, the direct BIE can be obtained in the time-domain as Equation (7) [68]:

$$c(\xi)u(\xi, t) = \int_{\Gamma_0 \cup \Gamma_1 \cup \cdots \cup \Gamma_n} \left\{ \int_0^t [u^*(x, t; \xi, \tau) \cdot q_j(x, t) - q^*(x, t; \xi, \tau) \cdot u_j(x, t)] d\tau \right\} d\Gamma(x), j$$

$$= 0, 1, 2, \cdots, n \tag{7}$$

In Equation (7), u^* and q^* are the half-space displacement and traction Green's functions of the time-domain, respectively; u_j and q_j are represent the displacements and traction

fields on the boundary, respectively; x and ξ are the coordinates of source and receiver, respectively; and Γ denotes the boundary. The Riemann-convolution integrals are shown by $u^* \cdot q_j$ and $q^* \cdot u_j$. The angle of boundary refraction is defined by $c(\xi)$, which is named as the geometry coefficient as well [69]. By inserting the free-field displacement on the surface of the half-plane with no subsurface irregularities, the BIE (7) can be rewritten as BIE (8) for the total displacement [36, 70].

$$c(\xi)u(\xi,t) = \int_{\Gamma_0 \cup \Gamma_1 \cup \cdots \cup \Gamma_n} \left\{ \int_0^t [u^*(x,t;\xi,\tau) \cdot q_j(x,t) - q^*(x,t;\xi,\tau) \cdot u_j(x,t)]d\tau \right\} d\Gamma(x)$$
$$+ u_0^{ff}(\xi,t), j = 0,1,2,\cdots,n \tag{8}$$

The free-field displacement on a surface without the presence of any irregularities is defined by u_0^{ff}. In this step, the total displacement in the presence of subsurface inclusions can be obtained by solving Equation (8) and it is possible to calculate displacements at any point m in Ω, including the ground surface ($y = 0$). To use the following modified equation for internal points, $c^m(\xi)$ should be equal to 1.0 as the following equation:

$$u^m(\xi,t) = \int_{\Gamma_0 \cup \Gamma_1 \cup \cdots \cup \Gamma_n} \left\{ \int_0^t [u^{*m}(x,t;\xi,\tau) \cdot q_j(x,t) - q^{*m}(x,t;\xi,\tau) \cdot u_j(x,t)]d\tau \right\} d\Gamma(x)$$
$$+ u_0^{ff.m}(\xi,t), j = 0,1,2,\cdots,n \tag{9}$$

where the half-space displacement and traction Green's functions for each internal point are represented by u^{*m} and q^{*m}, respectively. Additionally, $u^{ff.m}$ is the free-field displacements that should be recalculated in this step.

4. Numerical implementation

In this step, before solving Equation (8) and obtaining field variables, the geometric boundary of the body should be discretized and the time-axis should be considered. Equation (8) is an exact solution until reaching this step and there is no approximation in this equation before applying discretization on the boundaries of the multi-pitted medium and closed filled solids. To carry out temporal integration, an analytical process should be performed by a numerical procedure to achieve spatial integration. This process is presented in the following sections.

4.1. Temporal integration

When $t = N\Delta t$, the time interval will be divided into N equal increments by considering Δt from 0 to t. The field variables can be assumed to remain linearly within each time-step. Therefore, by applying temporal integrations, the time-convoluted BIE can be rewritten as Equation (10).

$$c(\xi)u^N(\xi) = \sum_{n=1}^{N} \int_{\Gamma_0 \cup \Gamma_1 \cup \cdots \cup \Gamma_n} \left(\begin{array}{c} [U_1^{N-n+1}(x,\xi)q_j^n(x) + U_2^{N-n}(x,\xi)q_j^n(x)] \\ -[Q_1^{N-n+1}(x,\xi)u_j^n(x) + Q_2^{N-n}(x,\xi)u_j^n(x)] \end{array} \right) d\Gamma(x)$$
$$+ u_0^{ff.N}(\xi), j = 0,1,2,\cdots,n \tag{10}$$

where U_1^{N-n+1} and U_2^{N-n} are the compact form of half-plane displacement time-convoluted kernels and Q_1^{N-n+1} and Q_2^{N-n} are the half-plane traction time-convoluted kernels. These kernels are shortened in the closed-form and correspond to the forward and backward time-nodes within a time-step. In Equation (10), u^N is the boundary displacement and $u^{ff.N}$ is the free-field displacement at the time $t = N\Delta t$. Moreover, the displacement and traction of boundary nodes are denoted by u_j^n and q_j^n, respectively. The full form of the kernels half-plane displacement and traction is presented in Panji et al. [22].

4.2. Spatial integration

To discretize the boundary of the domain for performing the spatial integration in numerical form, the isoparametric quadratic elements are utilized and all the related quantities to the geometry and field variables are given in terms of nodal variables. Thus, by considering the spatial discretization, the reformed shape of Equation (10) can be as Equation (11):

$$c(\xi)u^N(\xi) = \sum_{n=1}^{N}\sum_{m=1}^{M}\left[\begin{array}{l}\int_{\Gamma_0\cup\Gamma_1\cup...\cup\Gamma_n}[U_1^{N-n+1}(x(\kappa),\xi) + U_2^{N-n}(x(\kappa),\xi)]N_\alpha(\kappa)|J|d\kappa\,q_\alpha^n - \\ \int_{\Gamma_0\cup\Gamma_1\cup...\cup\Gamma_n}[Q_1^{N-n+1}(x(\kappa),\xi) + Q_2^{N-n}(x(\kappa),\xi)]N_\alpha(\kappa)|J|d\kappa\,u_\alpha^n\end{array}\right]$$
(11)

where the closed-form of scalar half-plane displacement and traction kernels are shown by $U_1^{N-n+1} + U_2^{N-n}$ and $Q_1^{N-n+1} + Q_2^{N-n}$, respectively; $u^{ff.N}$ and u^N present free-field motion and displacement field in time step N, respectively; u^n and q^n are displacement and traction vectors, respectively; $N_a(\kappa)$ is the quadratic shape functions, where κ is the local intrinsic coordinates of the elements. M denotes the boundary elements for each inclusion; Γ_m denotes the portion of boundary to the element m; and J is the Jacobian of transformation [69].

4.3. Time-stepping algorithm

After discretizing the geometry boundary of the problem by three-node quadratic elements and forming the spatial integration of Equation (11) for all BEs, the matrix form of this equation can be derived as follows:

$$\sum_{n=1}^{N}H_j^{N-n+1}\{u_j^n\} = \sum_{n=1}^{N}G_j^{N-n+1}\{q_j^n\} + \{u_0^{ff.N}\}, j = 0, 1, 2, \cdots, n$$
(12)

where the elements of H_j^{N-n+1} and G_j^{N-n+1} matrices can be obtained by integration over the boundary elements. $\{u_j^n\}$ and $\{q_j^n\}$ are the vectors of boundary nodal quantities at the time-step n. By applying the boundary conditions on the geometric boundaries of the model, the solvable form of Equation (12) can be achieved as follows:

$$[A_{j_1}^1]\{X_j^N\} = [B_{j_1}^1]\{Y_j^N\} + \{R_j^N\} + \{u_0^{ff.N}\}, j = 0, 1, 2, \cdots, n$$
(13)

where $\{X_j^N\}$ and $\{Y_j^N\}$ are the vectors including unknown and known boundary variables, respectively. The effects of past dynamic-history on the current time-node N is applied in

$\{R_j^N\}$. The equation for calculating $\{R_j^N\}$ is as follows:

$$\{R_j^N\} = \sum_{n=1}^{N-1}(G^{N-n+1}\{q^n\} - H^{N-n+1}\{u^n\}), j = 0, 1, 2, \cdots, n \tag{14}$$

After solving Equation (13), all boundary unknowns at each time-step and displacements at the internal point 'm' placed into the domain will be available.

5. Modeling

Based on the sub-structuring process, the subsurface inclusions are divided into two separate parts including a multi-pitted half-plane and a system of multiple closed filled solids. Figure 1 shows a schematic shape of this procedure. The modeling details are presented in the following sections.

5.1. Part I: multiple pitted half-plane

The first part includes a semi-infinite media with multiple hollow cavities subjected to the seismic *SH*-waves. If the interface nodes of the cavities connected to the surrounding domain are identified by the subscript of $0j$, the discretized BIE at the time step N can be written as follows:

$$H_{0j}^1 u_{0j}^N = G_{0j}^1 q_{0j}^N + R_{0j}^N + u_{0j}^{ff.N}, \quad j = 1, 2, \cdots, n \tag{15}$$

where u_{0j}^N and q_{0j}^N are displacement and traction fields of the interface, respectively; R_{0j}^N is the past dynamic time-history of the interface in step N that is defined using Equation (16); and $u_{0j}^{ff.N}$ is the free-field motion of interface nodes.

$$R_{0j}^N = \sum_{n=1}^{N-1}(G_{0j}^{N-n+1}q_{0j}^n - H_{0j}^{N-n+1}u_{0j}^n), \quad j = 1, 2, \cdots, n \tag{16}$$

5.2. Part II: multiple closed filled solids

The second part includes a system of multiple closed alluvial solids as the filler materials of inclusions. If the interface nodes are identified by the subscript of $j0$, the discretized BIE at the time step N can be written as follows:

$$H_{j0}^2 u_{j0}^N = G_{j0}^2 q_{j0}^N + R_{j0}^N, \quad j = 1, 2, \cdots, n \tag{17}$$

where, u_{j0}^N and q_{j0}^N are displacement and traction fields of the interface, respectively, and R_{j0}^N is the past dynamic time-history of the interface in step N, which is defined using Equation (18).

$$R_{j0}^N = \sum_{n=1}^{N-1}(G_{j0}^{N-n+1}q_{j0}^n - H_{j0}^{N-n+1}u_{j0}^n), \quad j = 1, 2, \cdots, n \tag{18}$$

5.3. Assembling

To solve the problem and determining unknown variables of interfaces, the needed equilibrium conditions of displacement and traction compatibility on the interfaces are as follows:

$$u_{0j}^N = u_{j0}^N, \quad j = 1, 2, \cdots, n \tag{19}$$

also

$$\mu_0 q_{0j}^N = -\mu_j q_{j0}^N, \quad j = 1, 2, \cdots, n \tag{20}$$

In these equations, μ_0 and μ_j are the shear modulus of the surrounding medium and multiple inclusions, respectively. After satisfying the mentioned conditions on interfaces, the final matrix form of the assembled BIEs will be as Equation (21). By solving this equation, all unknown variables of the interfaces, such as displacements and tractions can be obtained. By applying $c(\xi) = 1.0$ in the equations of the first part, the displacements of the ground surface can be calculated.

$$
\begin{bmatrix}
H_{01}^1 & -1/\mu_0 G_{01}^1 & H_{02}^1 & -1/\mu_0 G_{02}^1 & \cdots & H_{0n}^1 & -1/\mu_0 G_{0n}^1 \\
H_{10}^1 & -1/\mu_1 G_{10}^1 & 0 & 0 & \cdots & 0 & 0 \\
0 & 0 & H_{20}^1 & -1/\mu_2 G_{20}^1 & \cdots & 0 & 0 \\
\vdots & \vdots & \vdots & \vdots & \ddots & \vdots & \vdots \\
0 & 0 & 0 & 0 & \cdots & H_{n0}^1 & -1/\mu_n G_{0n}^1
\end{bmatrix}
\begin{Bmatrix}
u_{01}^N \\
q_{01}^N \\
u_{02}^N \\
q_{02}^N \\
\vdots \\
u_{0n}^N \\
q_{0n}^N
\end{Bmatrix}
$$

$$
= \begin{Bmatrix}
R_{0j}^N \\
R_{10}^N \\
R_{20}^N \\
\vdots \\
R_{n0}^N
\end{Bmatrix}
+ \begin{Bmatrix}
u_{0j}^{ff.N} \\
0 \\
0 \\
\vdots \\
0
\end{Bmatrix}, \quad j = 1, 2, \ldots, n \tag{21}
$$

6. The DASBEM program

Dynamic Analysis of Structures by Boundary Element Method (DASBEM) is a program based on the half-plane BEM prepared for the dynamic analysis of plane scalar time-domain problems. This program is developed for seismic analysis of 2D multiple subsurface circular/elliptical inclusions located in an elastic half-plane. The flowchart and the details of this program are presented in Panji et al. [64].

7. Application examples

By implementing the above formulation in the DASBEM algorithm, some practical examples are solved to examine the validity and efficiency of the proposed program. In the following sections, the Normalized Displacement Amplitude (NDA) is defined as the ratio of the Fourier amplitude of the total ground surface motion obtained by BEM for a defined frequency to the Fourier amplitude of the incident motion for the defined frequency. The

dimensionless frequency (η) is as ($\eta = \omega b/\pi c$), where ω is the angular frequency of the wave, b is the radius of inclusions, and c is the shear-wave velocity. The impedance ratio (I), as the stiffness ratio of inclusions material to the surrounding medium, is defined as ($I = \rho_i c_i/\rho_m c_m$), where ρ_i and c_i are the mass density and shear-wave velocity of inclusions, respectively, and ρ_m and c_m are mentioned parameters for the surrounding medium, respectively. Moreover, the amplification is the ratio of the surface response amplitude to free-field motion. The numerical procedure is implemented in the MATLAB [71] programming software.

To study the behavior of multiple underground inclusions located in an elastic half-plane subjected to the seismic SH-waves, some key parameters such as the number of inclusions, angle of incident waves, and the shape of inclusions are considered in the numerical study. The number of inclusions is between 2 and 16. Also, the angles (θ) of 0°, 30°, 60°, and 90° are applied for incidence waves. The impedance ratio (I) is equal to 0.333 and the shape of inclusions is defined in circular and elliptical mode with SR = 0.5. First, to illustrate the propagation and diffraction of the incident waves on the ground surface, the responses of time-domain are presented. Then, by showing the 3D frequency-domain results, the general pattern of amplification and displacements of the ground surface are demonstrated. In the last part, the propagation of incidence waves below the ground surface is illustrated by some snapshots for specific cases at different times.

7.1. Verification study

To compare the obtained responses with the solutions presented by other researchers, some examples are considered in the following. The verification examples are prepared based on the models of two and nine circular subsurface inclusions subjected to vertical and horizontal incidence waves angle. The details are described in the following subsections.

7.1.1. Twin circular inclusions

As depicted in Figure 2, twin circular inclusions are modeled in the depth of 2b subjected to incident SH-waves and the obtained responses are compared with those presented by Dravinski & Yu [72]. These researchers applied the direct full-plane frequency-domain BIE approach to show the ground surface displacements. The dimensionless frequency (η) of 0.5 and the impedance ratio (I) of 0.333 and the vertical (0°) and horizontal (90°) incident waves are applied in the model. The range of ground surface is between $-10b$ and $10b$ and the length ratio (LR) between the center of inclusions is equal to 6. The shear-wave velocity (c_j) and the mass density (ρ_j) of 600 m.s^{-1} and 0.667 ton.m^{-3} for the inclusions and 1200 m.s^{-1} and 1.0 ton.m^{-3} are considered for the surrounding medium, respectively. Additionally, the predominant frequency and maximum amplitude of the SH-waves of the Ricker wavelet type are equal to 3 Hz and 0.001 m, respectively. The problems are solved by 500 time-steps with Δt of 0.012 sec and the time-shifting parameter of 1.5 sec. The number of boundary elements considered for each circular inclusion is 94 elements. As shown in Figure 2, the obtained results of the present study for the model of twin inclusions and the solutions presented by Dravinski & Yu [72] illustrate a good agreement such that the diagrams are completely coincident.
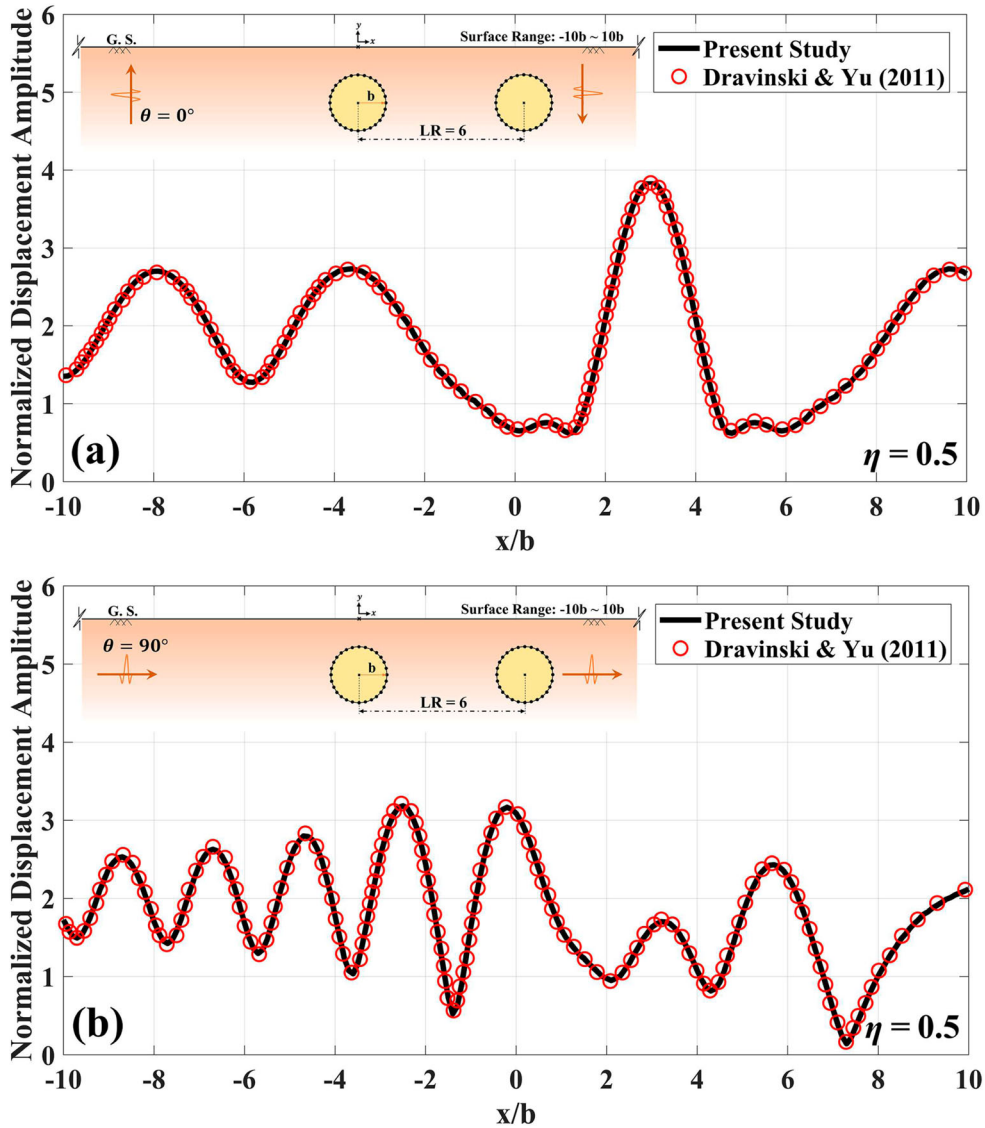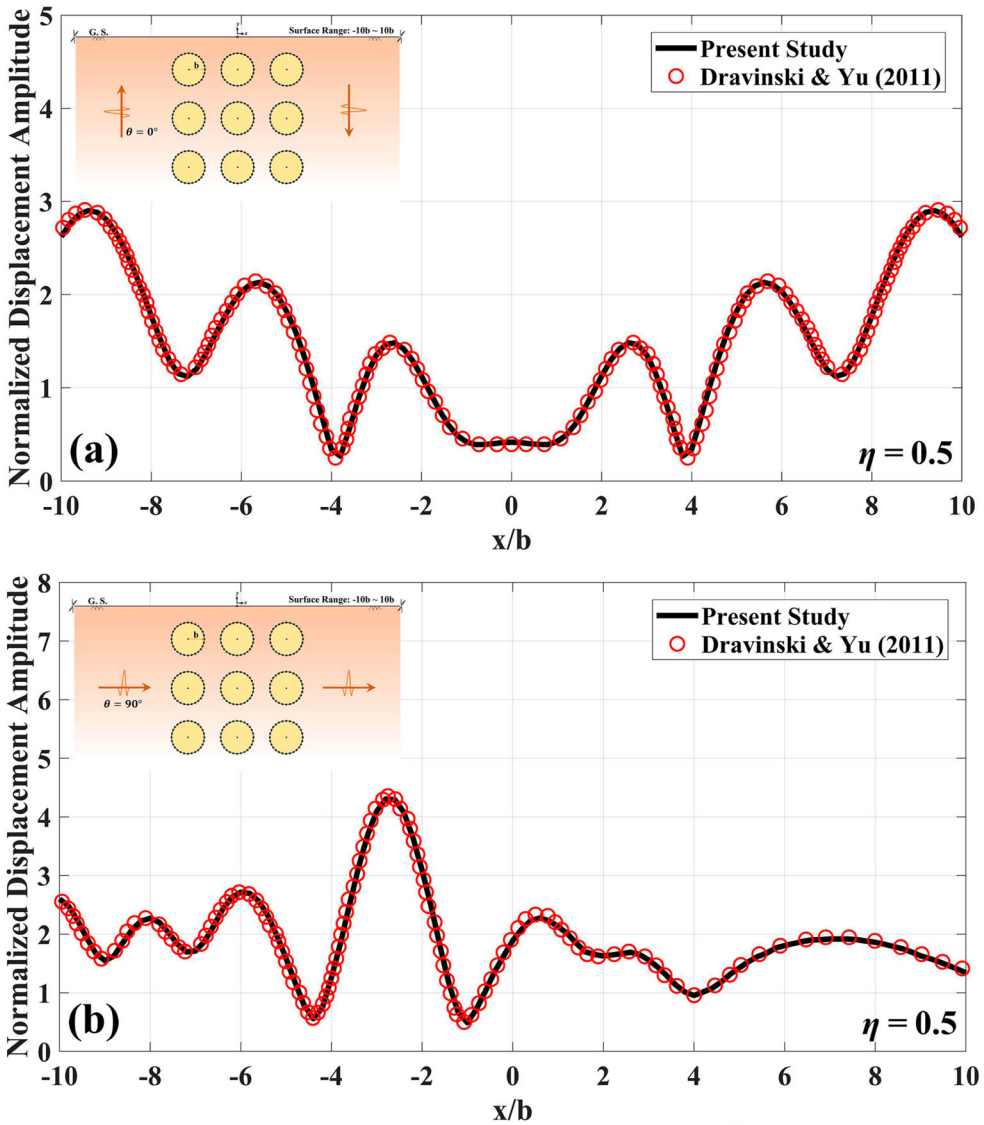
Figure 2. The normalized displacement amplitude of the ground surface versus x/b for the model of twin circular inclusions subjected to the *SH*-waves. The dimensionless frequency of $\eta = 0.5$ for the incident angle of (a) $\theta = 0°$ and (b) $\theta = 90°$.

7.1.2. Nine circular inclusions

Figure 3 presents the obtained results of the present study for nine subsurface circular inclusions compared to the solutions presented by Dravinski & Yu [72]. The rows of inclusions are located in the depth ratios (DR) of 2, 5 and 8 subjected to the incident angles of (θ) of 0° and 90°. The other effective parameters are considered similar to those of the previous example. Comparing the diagrams shows a good agreement and demonstrates the appropriate ability and high accuracy of the proposed program for modeling and analysis of complex subsurface filled underground features.

Figure 3. The normalized displacement amplitude of the ground surface versus x/b for the model of nine circular inclusions subjected to the *SH*-waves. The dimensionless frequency of $\eta = 0.5$ for the incident angle of (a) $\theta = 0°$ and (b) $\theta = 90°$.

7.2. Time-domain responses

Figures 4–7 illustrate the general pattern of responses in time-domain and demonstrate the scattering of the *SH*-waves in the presence of a system of multiple circular inclusions. For a better interpretation of the results, four types of stations are marked on the figures by the signs D, R, C, and R_t to separate the different phases of scattered waves. The direct paths of waves that move to the surface are shown by D. After the collision of the waves to the boundary of inclusions, a significant part of the waves is reflected directly, which is indicated by R sign. The other phase, which is related to creeper waves, is marked by C sign.
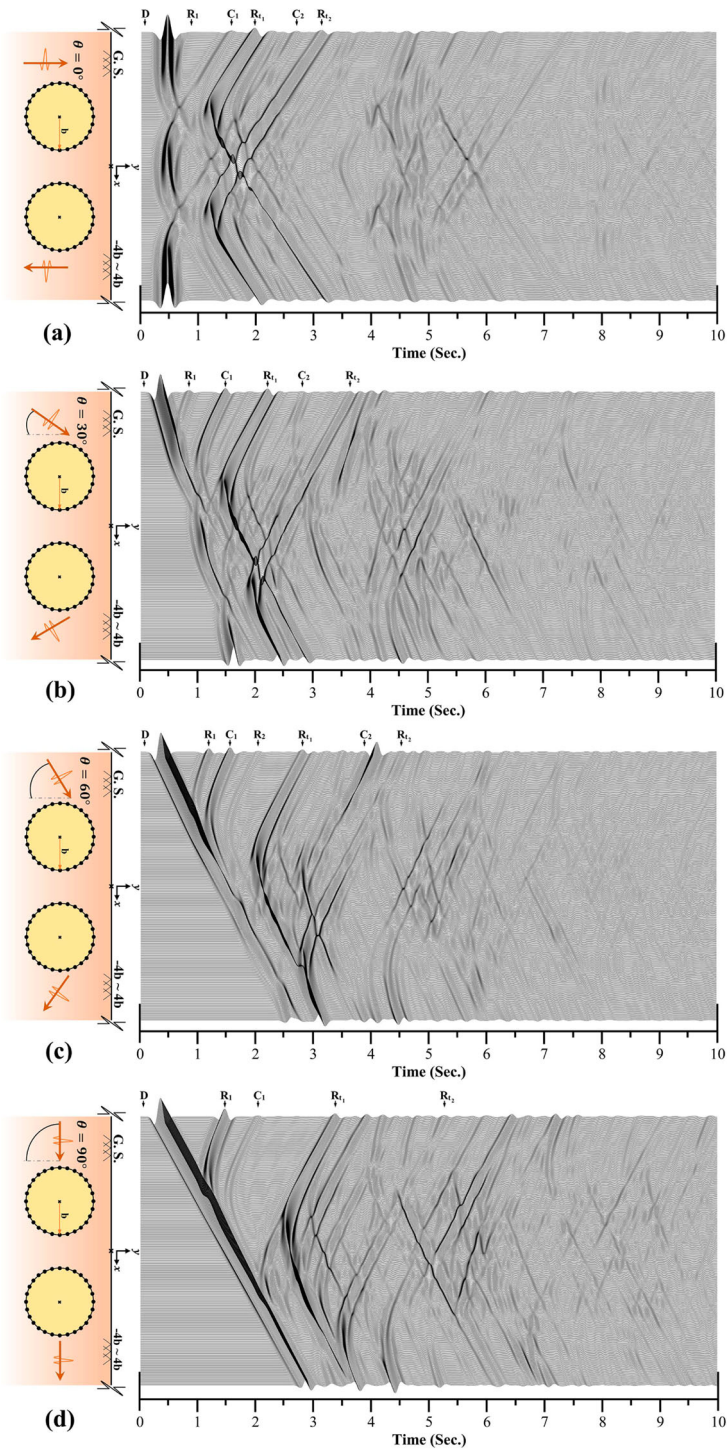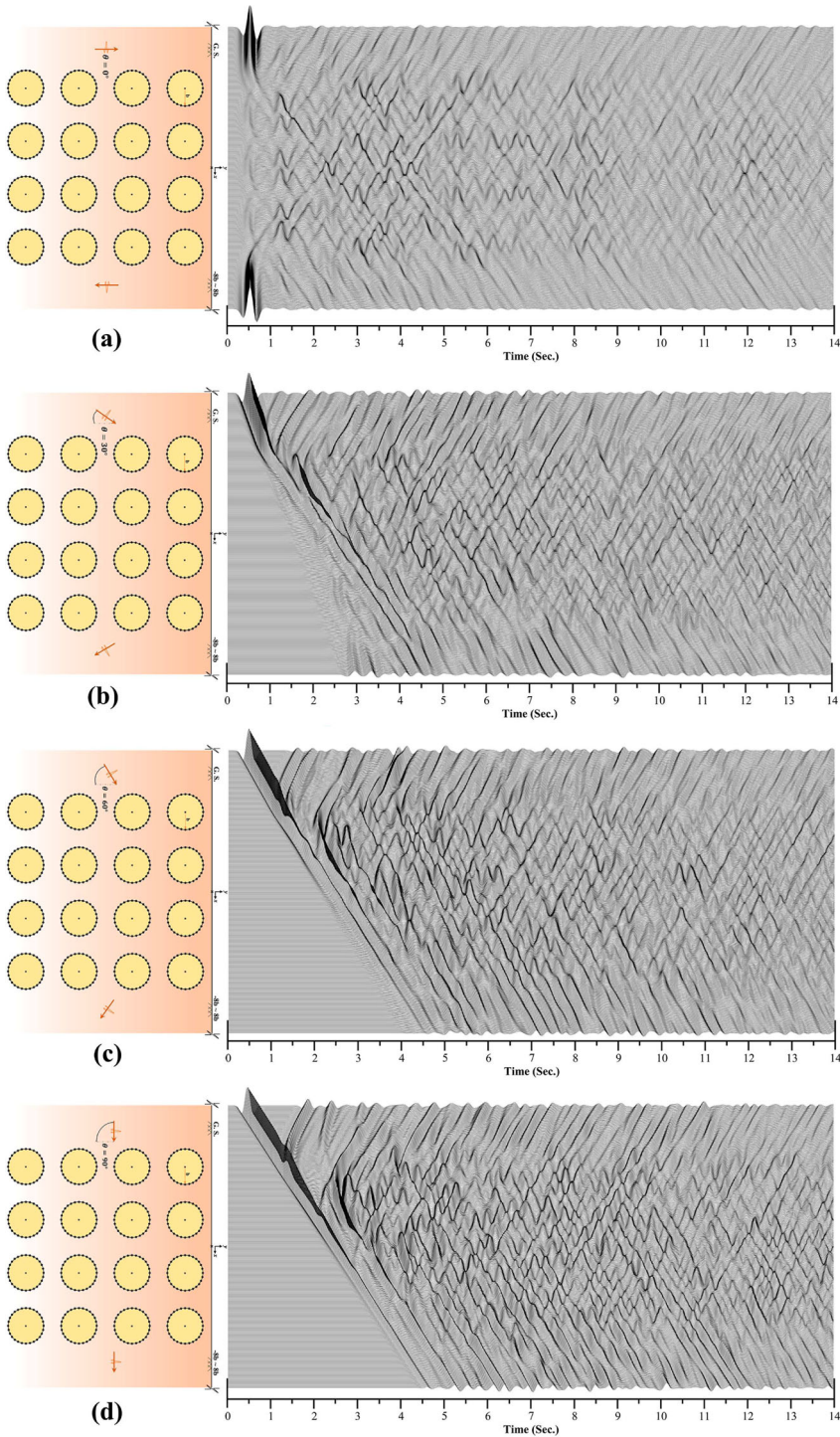
Figure 4. Synthetic seismograms of the ground surface and the procedure of the *SH*-waves dispersion with time, for the model of twin circular inclusions and the incident angle of (a) $\theta = 0°$, (b) $\theta = 30°$, (c) $\theta = 60°$ and (d) $\theta = 90°$.
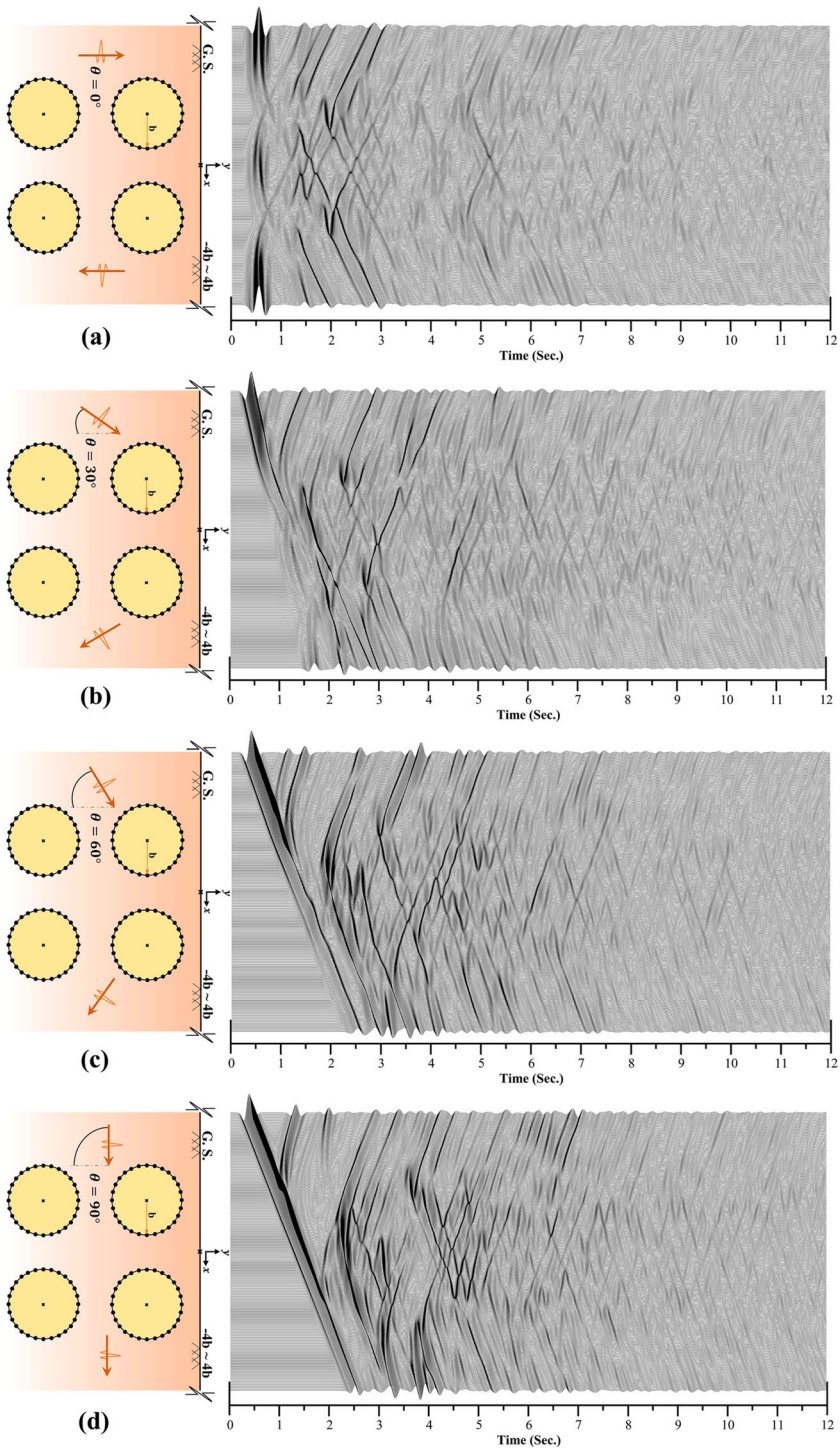
Figure 5. Synthetic seismograms of the ground surface and the procedure of the *SH*-waves dispersion with time, for the model of four circular inclusions in two row and the incident angle of (a) $\theta = 0°$, (b) $\theta = 30°$, (c) $\theta = 60°$ and (d) $\theta = 90°$.
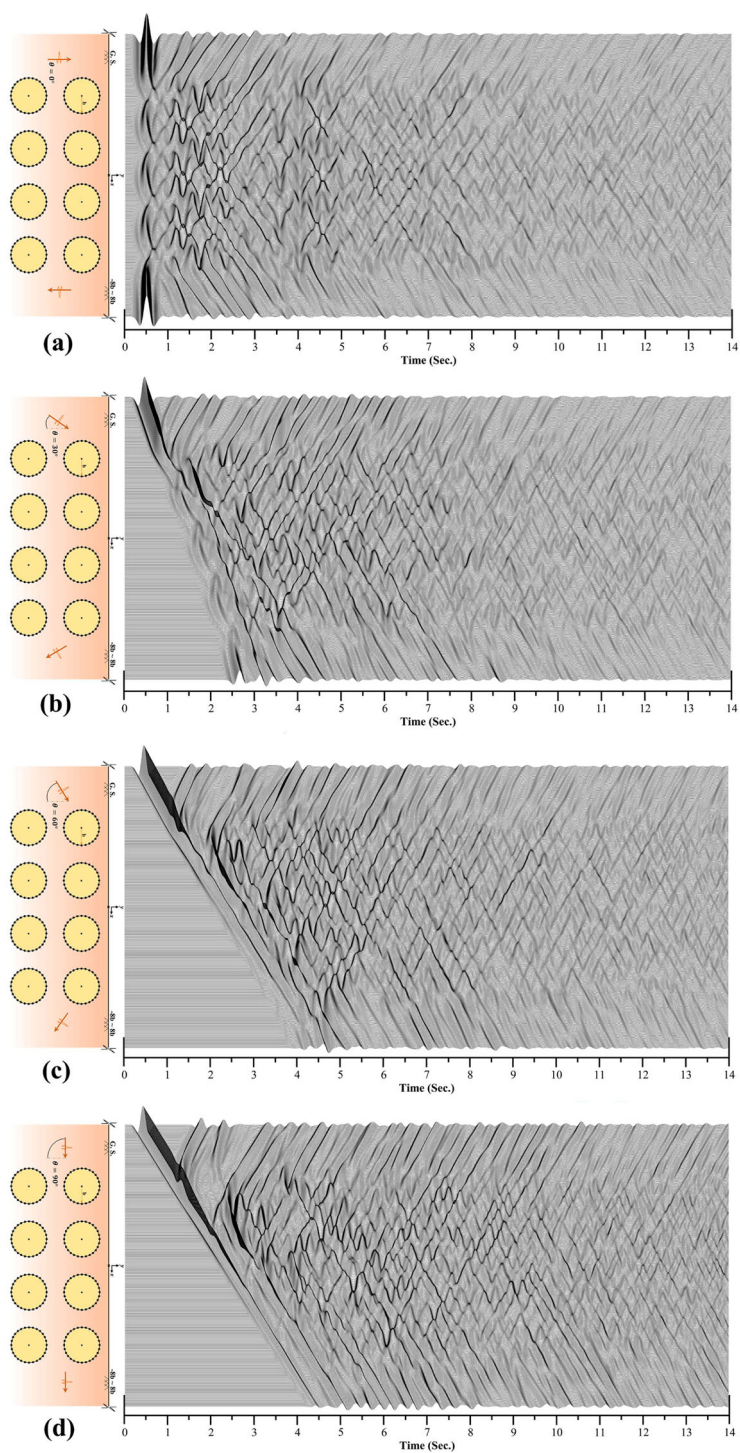
Figure 6. Synthetic seismograms of the ground surface and the procedure of the *SH*-waves dispersion with time, for the model of eight circular inclusions and the incident angle of (a) $\theta = 0°$, (b) $\theta = 30°$, (c) $\theta = 60°$ and (d) $\theta = 90°$.

Figure 7. Synthetic seismograms of the ground surface and the procedure of the *SH*-waves dispersion with time, for the model of 16 circular inclusions and the incident angle of (a) $\theta = 0°$, (b) $\theta = 30°$, (c) $\theta = 60°$ and (d) $\theta = 90°$.

These waves are crawling on the boundary of inclusions and then reflected after hitting the surface. Based on the considered impedance ratio ($I = 0.333$), the stiffness of inclusions materials is 66.7% softer than the surrounding medium. Because of the weaker material of inclusions compared to the main domain, most parts of incident waves are trapped inside the inclusions. Also, the boundary of inclusions acts like a mirror and does not allow the trapped waves to leave the medium quickly. Additionally, some remaining parts of reflected and crawler waves in the domain are trapped, and consecutively reflected between the inclusions and ground surface. The mentioned phases are marked by R_t [73]. The number of subscripts is shown the related phases to each of the inclusions.

Figure 4 shows the time history responses of twin circular inclusions. As can be seen, when $\theta = 0°$ (Figure 4(a)), the result is completely symmetric and the inclination of the wave-front causes the disappearance of symmetry. The amplitudes are reduced behind the location of inclusions relative to the direction of the wave-front. This phenomenon shows that the existence of inclusions leads to scattering and especially absorption the most part of incoming waves and causes a shadow zone effect behind the inclusions [74]. The absorbed waves are trapped inside the inclusions and experience intermittent reflections with more delay, which increases the duration of convergence time. Moreover, the highest volume of trapped waves emerges (Figure 4(a)) because of direct waves collision to the inclusions. Meanwhile, Figure 4(b,c) show the stronger role of inclusions in the deviation of the waves from their initial paths and blocking their paths to the surface. In circular-shaped inclusions, the incidence waves can easily creep on the boundaries because of the rotary section of inclusions and the amplitude of crawler waves (C) is higher than the reflected phase (R). The details are more visible for incidence angles of 30° and 60°. In Figure 4(d), the effect of the crawler waves on the ground surface is significantly reduced and the inclusions block the paths of the waves behind the first inclusion. At the point of waves collision to the first inclusion, the existence of inclusion does not allow the waves to cross easily and reach the behind side of inclusion relative to the angle of the incidence waves and acts as a barrier. Although the second inclusion touches a lower volume of direct waves, a significant volume of reflected waves hits the surface and then is trapped between the top boundaries of inclusions and ground surface. Therefore, the vibrations are still visible over time. Figure 5 shows the model of four circular inclusions placed in two rows. As can be seen, the oscillations of the responses are more than the model of twin inclusions (Figure 4). The volume of trapped waves is higher and the contribution of reflected and crawler phases are stronger. For this reason, the convergence time is prolonged. A closer look at Figure 5(a) shows that in the vertical angle of waves, the most part of waves is reflected and trapped immediately by the inclusions embedded in the second row. Therefore, the contribution of inclusions in the first row is decreased and the vibrations of diagrams are diminished. In Figure 5(b), the existence of inclusions helped the waves to leave the medium faster. Also, an appropriate crawler and reflection phases are observed in Figure 5(c,d), suggesting the severe reflections on the boundaries placed in front of the wave-front. In the following, the results of 8 and 16 circular inclusions are presented. The high intricacy of the time-domain responses for the mentioned models makes it very difficult to determine the individual phases of incidence waves on the surface exactly.

Figures 8–11 show the waves scattering patterns in the presence of multiple elliptical inclusions. When the inclusions are elliptical, the volume of trapped waves is decreased. But, more iterative reflections of trapped waves occur with a shorter delay, which is because
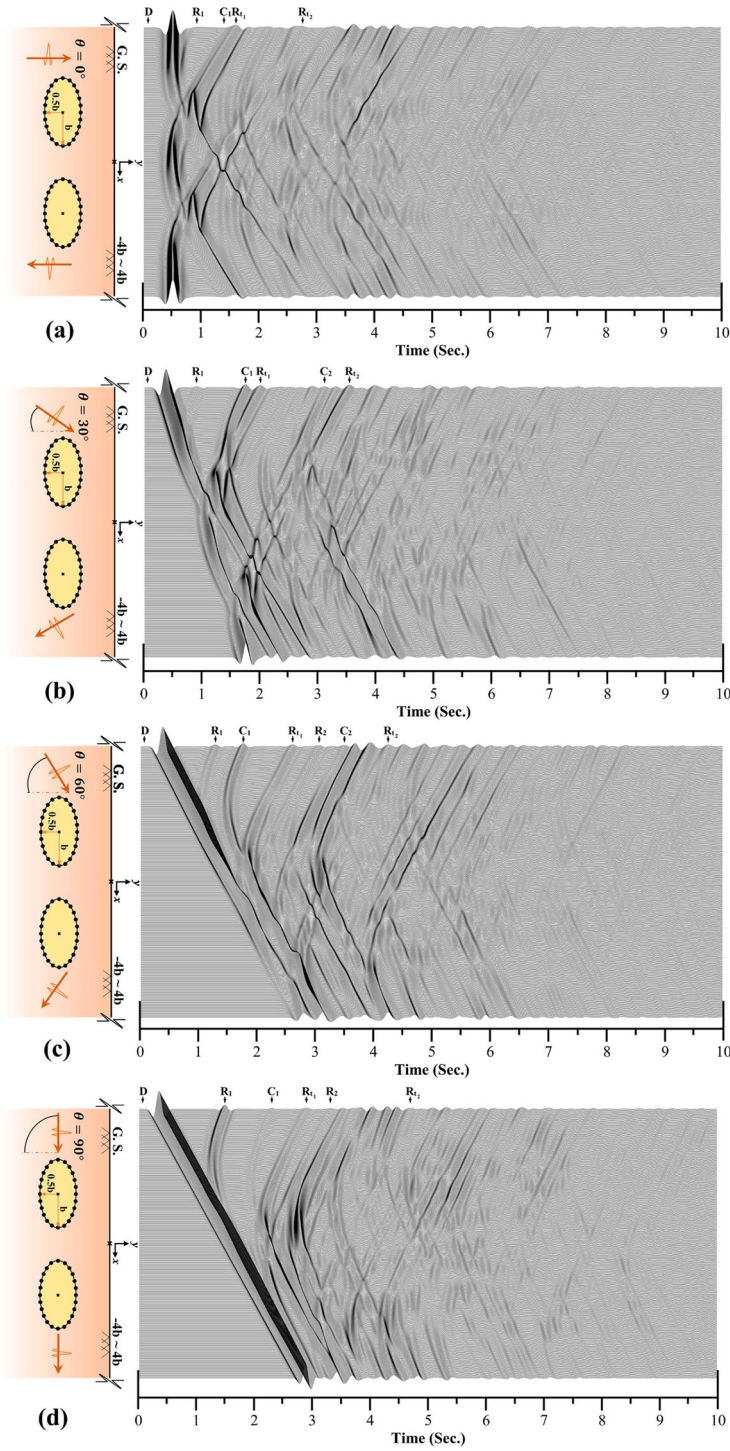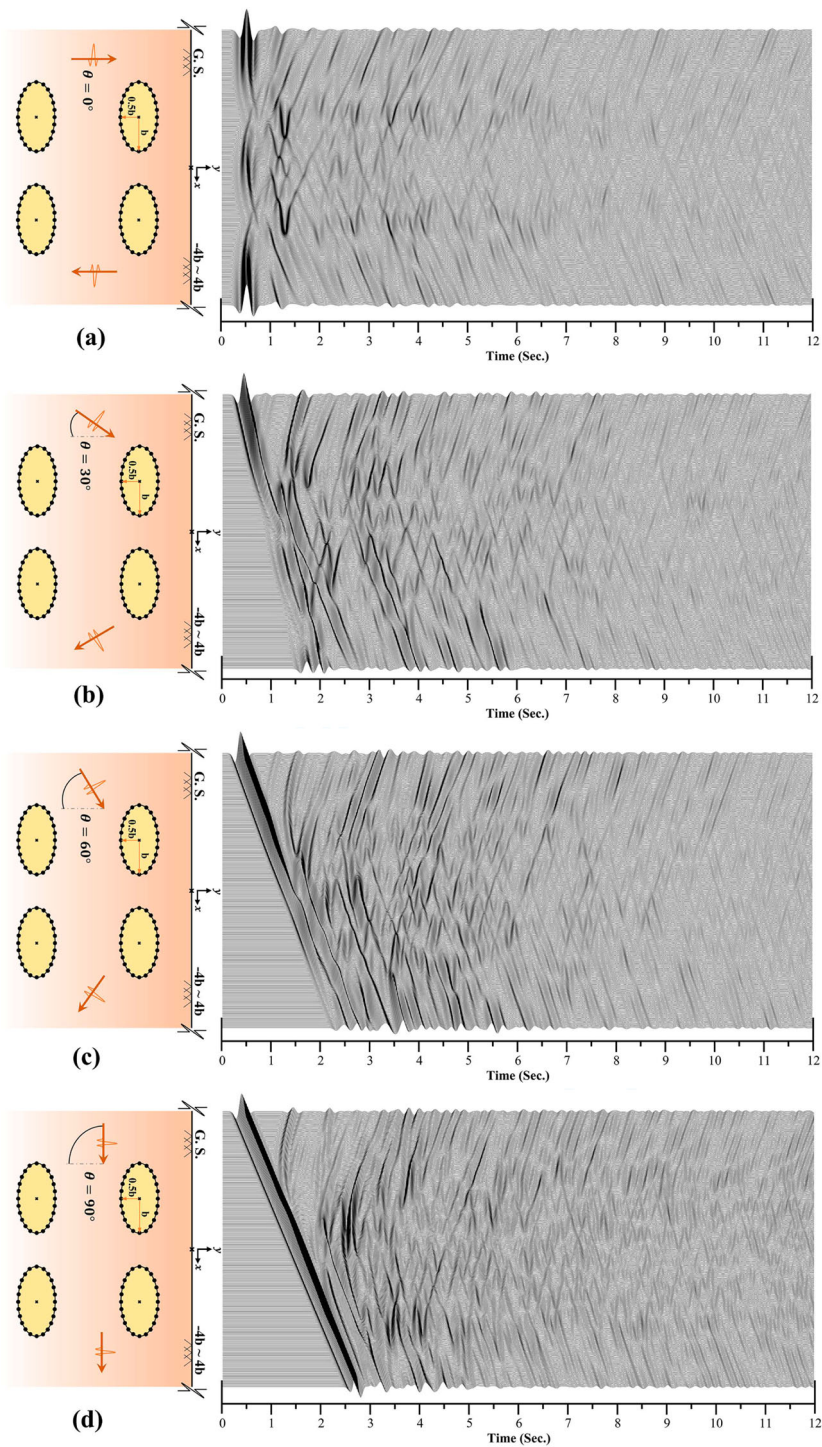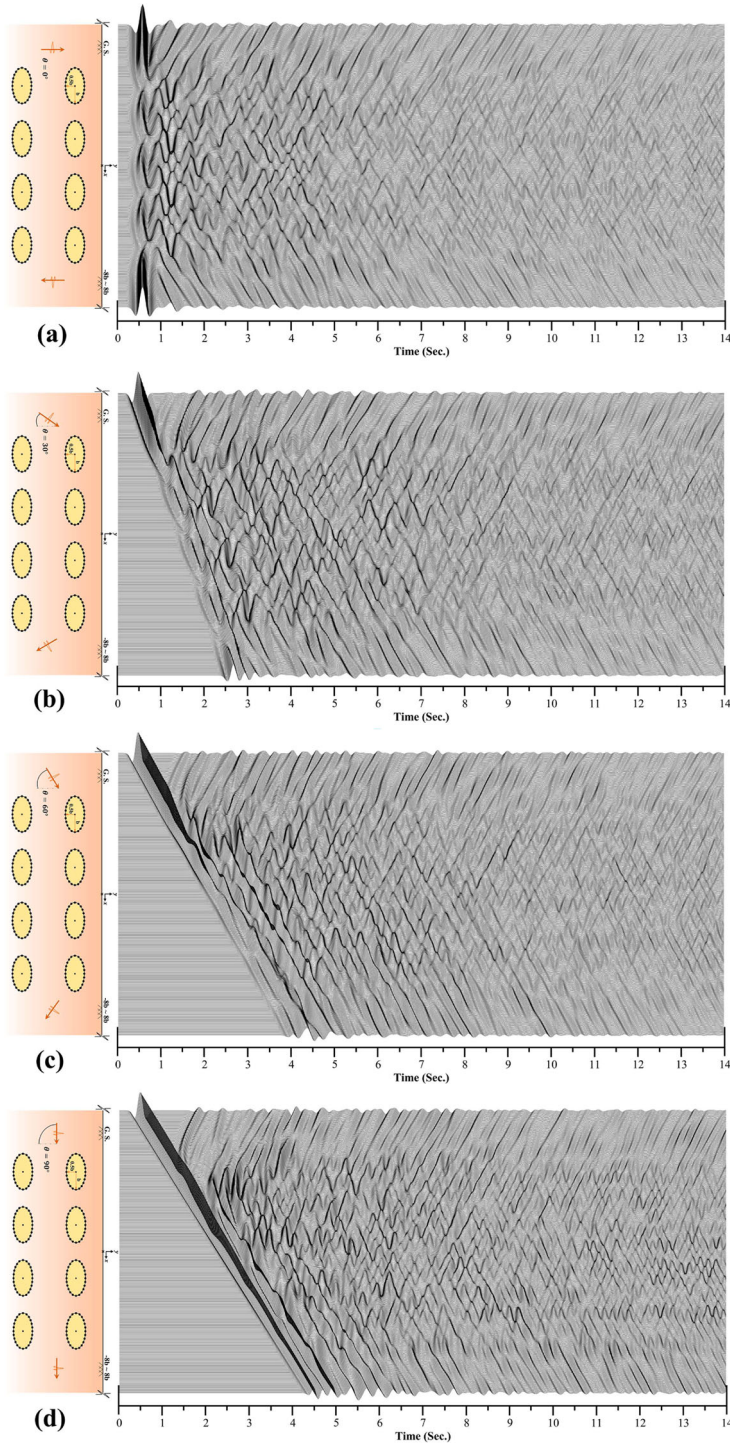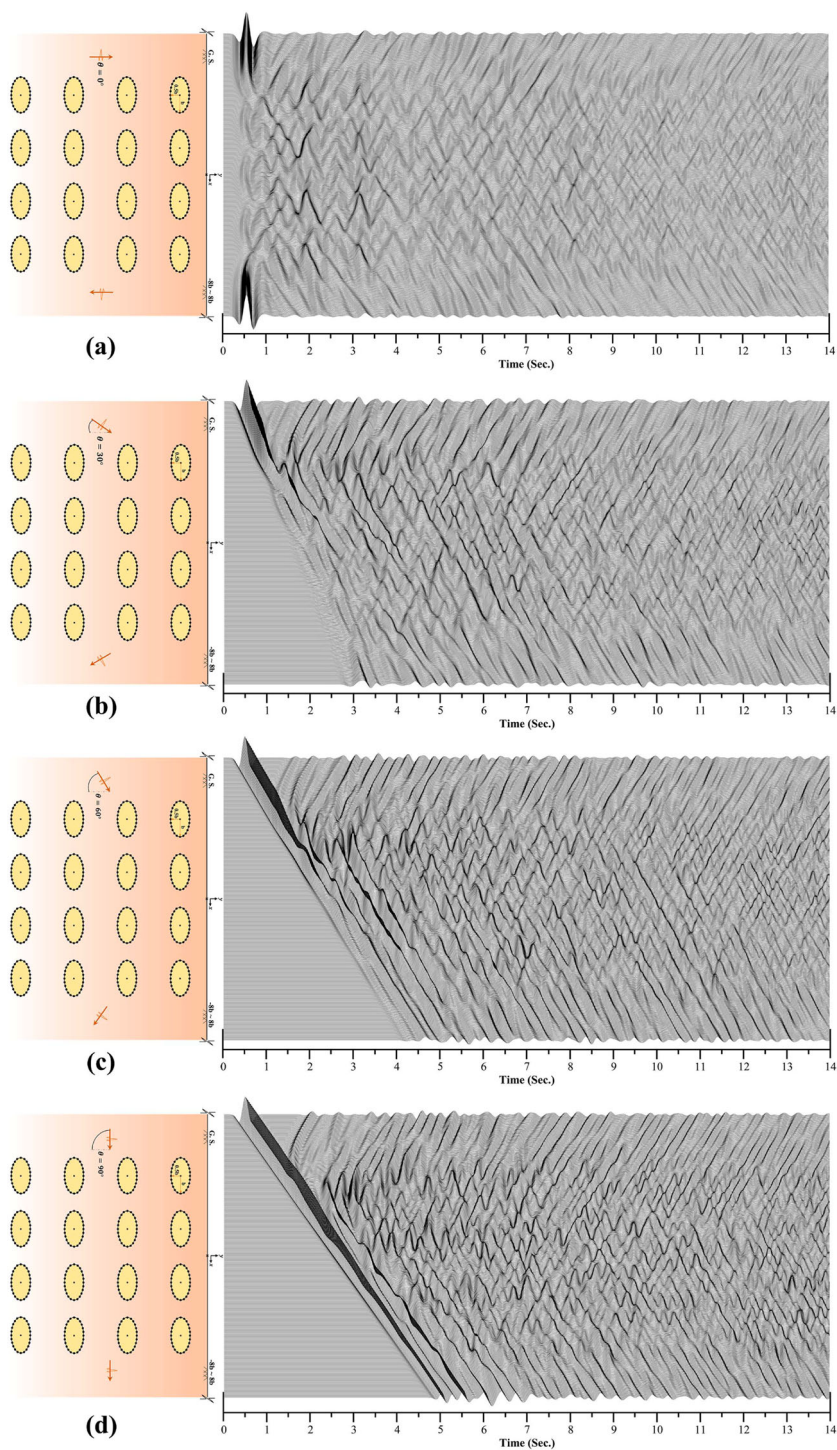
Figure 8. Synthetic seismograms of the ground surface and the procedure of the *SH*-waves dispersion with time, for the model of twin elliptical inclusions and the incident angle of (a) $\theta = 0°$, (b) $\theta = 30°$, (c) $\theta = 60°$ and (d) $\theta = 90°$.

**Figure 9.** Synthetic seismograms of the ground surface and the procedure of the *SH*-waves dispersion with time, for the model of four elliptical inclusions in two rows and the incident angle of (a) $\theta = 0°$, (b) $\theta = 30°$, (c) $\theta = 60°$ and (d) $\theta = 90°$.

Figure 10. Synthetic seismograms of the ground surface and the procedure of the *SH*-waves dispersion with time, for the model of eight elliptical inclusions and the incident angle of (a) $\theta = 0°$, (b) $\theta = 30°$, (c) $\theta = 60°$ and (d) $\theta = 90°$.

Figure 11. Synthetic seismograms of the ground surface and the procedure of the *SH*-waves dispersion with time, for the model of 16 elliptical inclusions and the incident angle of (a) $\theta = 0°$, (b) $\theta = 30°$, (c) $\theta = 60°$ and (d) $\theta = 90°$.
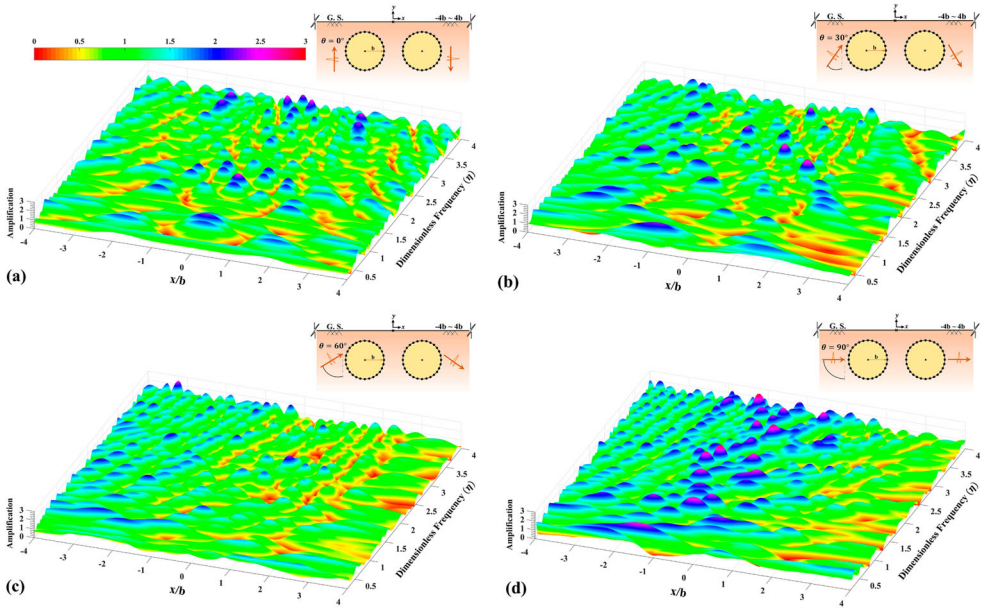
Figure 12. The 3D amplification of the ground surface versus different dimensionless frequencies for the model of twin circular inclusions subjected to the *SH*-waves and the incident angle of (a) $\theta = 0°$, (b) $\theta = 30°$, (c) $\theta = 60°$, and (d) $\theta = 90°$.

of the smaller medium of inclusions. The continuous fluctuations in a short period of time can be observed in the responses. Like the previous cases, the wave absorption by inclusions reduced the amplitudes of waves right above their locations. Moreover, the specific shape of elliptical inclusions diminishes the amplitude of crawler waves and the trapped waves between the inclusions and the ground surface. In Figure 8(a), the collision of vertical waves to the below boundary of the inclusions induces the barrier effect of inclusions stronger than the circular models such that the waves cannot crawl on the boundaries and reach the surface suitably. In Figure 8(b), a significant portion of the waves can creep along the boundaries and the amplitude of reflected waves is very lower compared to the similar circular model (Figure 4(b)). When the incidence angle is 60° (Figure 8(c)), the crawler phase is formed easier. Also, in Figure 8(d), the effect of the shadow zone behind the inclusions is weakened. In the following, the responses of 8 and 16 elliptical inclusions are presented.

7.3. Frequency-domain responses

Presenting the results of frequency-domain is the only possible way to illustrate the general pattern of surface displacements subjected to seismic waves. Figures 12–15 demonstrate the 3D amplification patterns in the presence of multiple circular inclusions. In the model of twin circular inclusions with $\theta = 0°$ (Figure 12(a)), the response is symmetric and one can see low amplifications in the location of inclusions, which is because of wave absorption by the inclusions. The collision of the incident waves to the boundary of inclusions separated the direct waves to reflected and refracted phases of waves. A portion of the reflected waves leaves the medium and another portion deviates from its initial paths and reaches
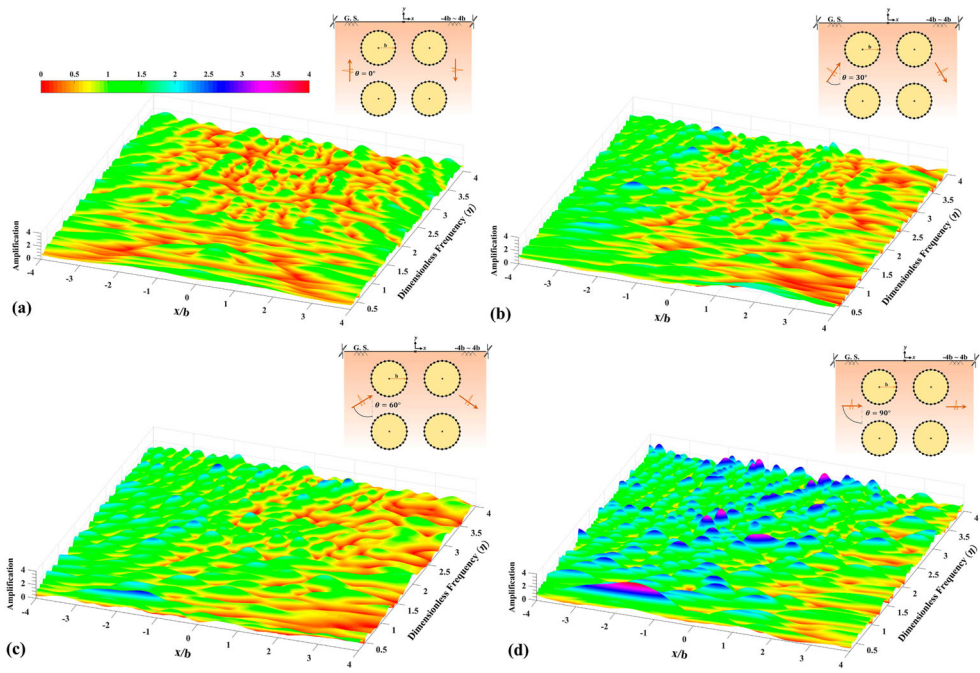
Figure 13. The 3D amplification of the ground surface versus different dimensionless frequencies for the model of four circular inclusions in two rows subjected to the *SH*-waves and the incident angle of (a) $\theta = 0°$, (b) $\theta = 30°$, (c) $\theta = 60°$, and (d) $\theta = 90°$.
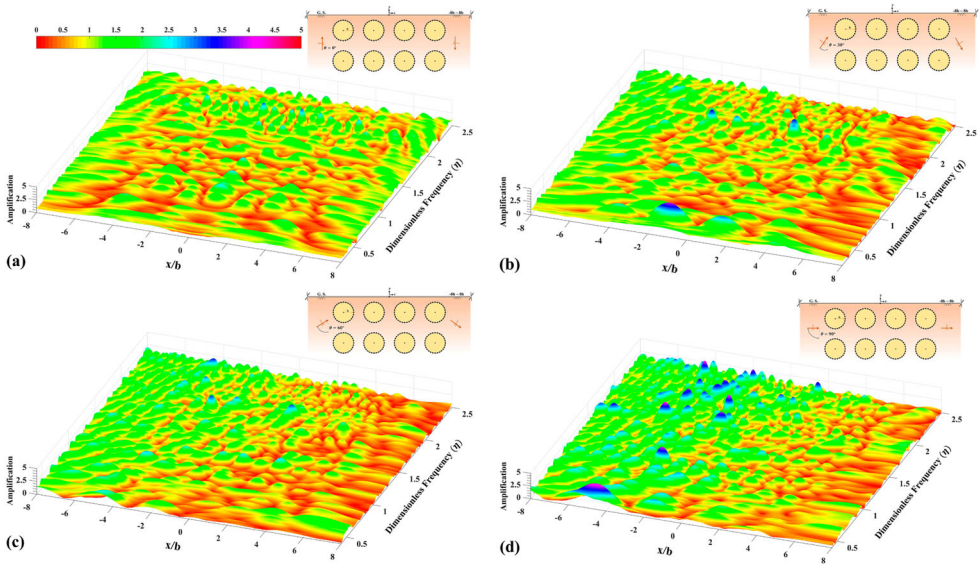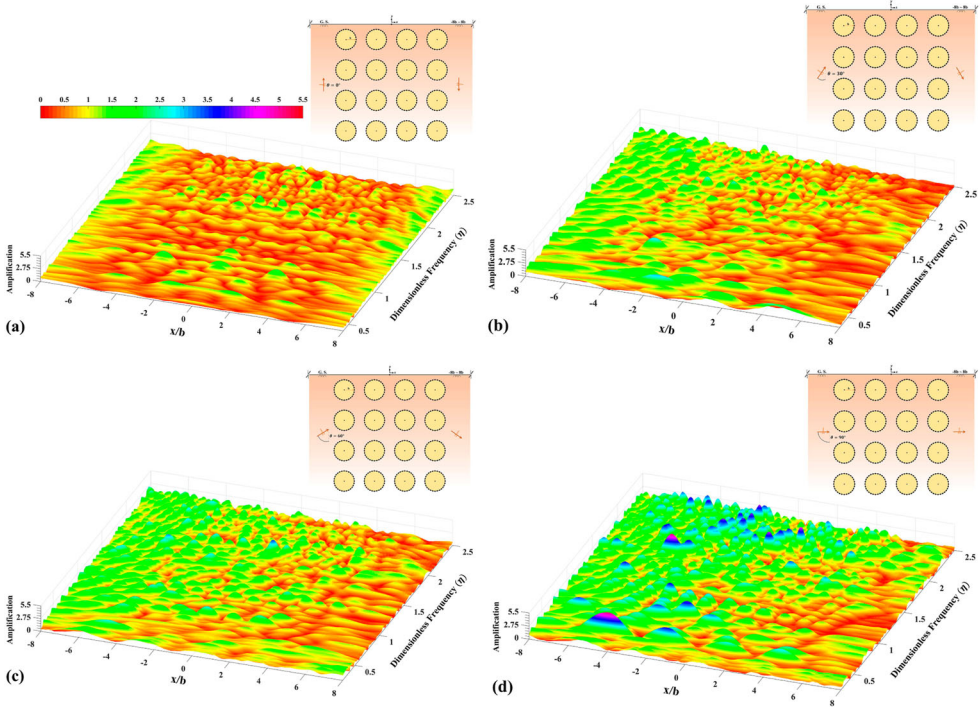

Figure 14. The 3D amplification of the ground surface versus different dimensionless frequencies for the model of eight circular inclusions subjected to the *SH*-waves and the incident angle of (a) $\theta = 0°$, (b) $\theta = 30°$, (c) $\theta = 60°$, and (d) $\theta = 90°$.

Figure 15. The 3D amplification of the ground surface versus different dimensionless frequencies for the model of 16 circular inclusions subjected to the *SH*-waves and the incident angle of (a) $\theta = 0°$, (b) $\theta = 30°$, (c) $\theta = 60°$, and (d) $\theta = 90°$.
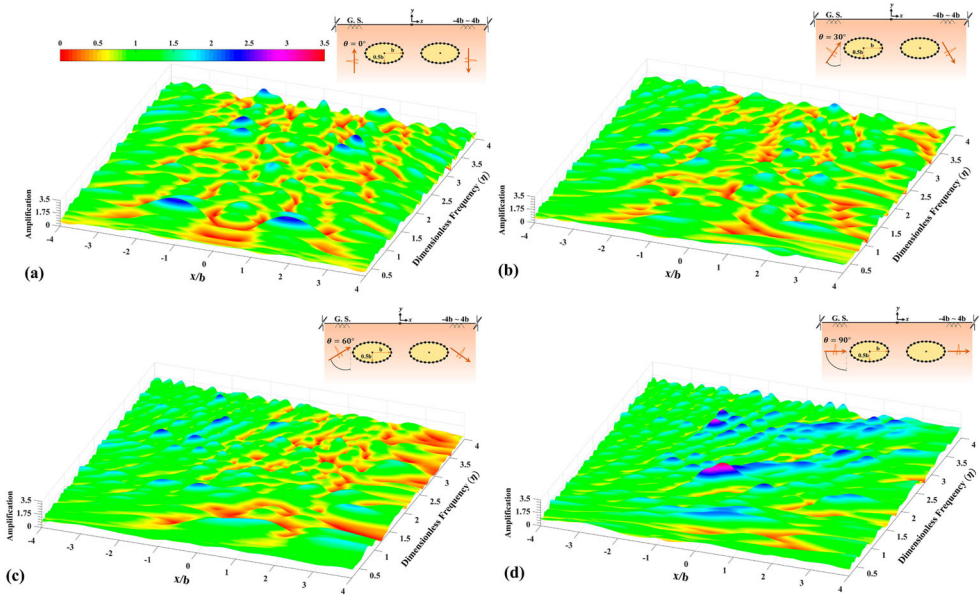

Figure 16. The 3D amplification of the ground surface versus different dimensionless frequencies for the model of twin elliptical inclusions subjected to the *SH*-waves and the incident angle of (a) $\theta = 0°$, (b) $\theta = 30°$, (c) $\theta = 60°$, and (d) $\theta = 90°$.
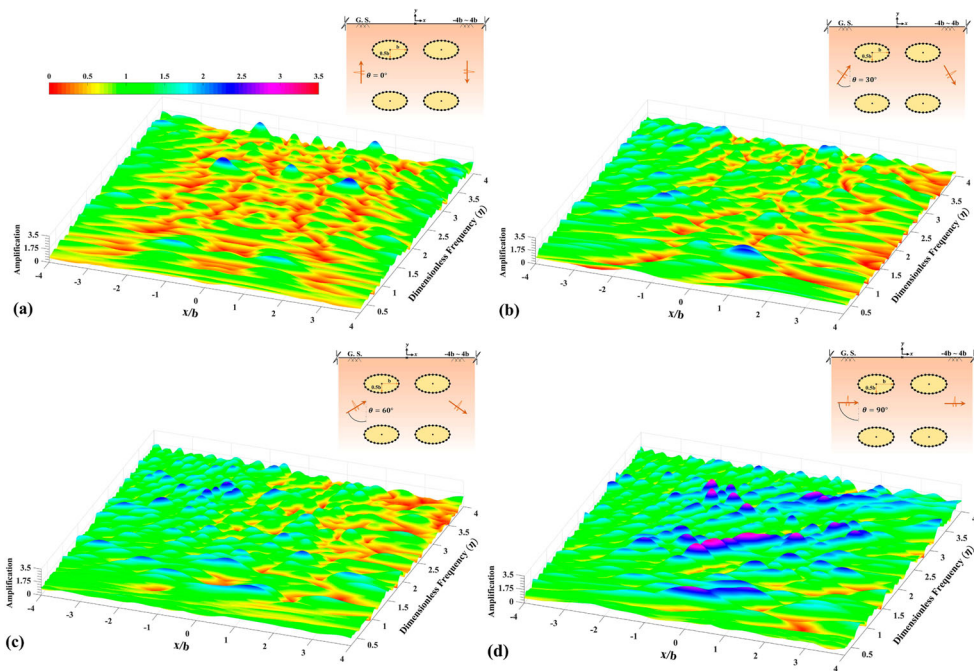
Figure 17. The 3D amplification of the ground surface versus different dimensionless frequencies for the model of four elliptical inclusions in two rows subjected to the *SH*-waves and the incident angle of (a) $\theta = 0°$, (b) $\theta = 30°$, (c) $\theta = 60°$, and (d) $\theta = 90°$.
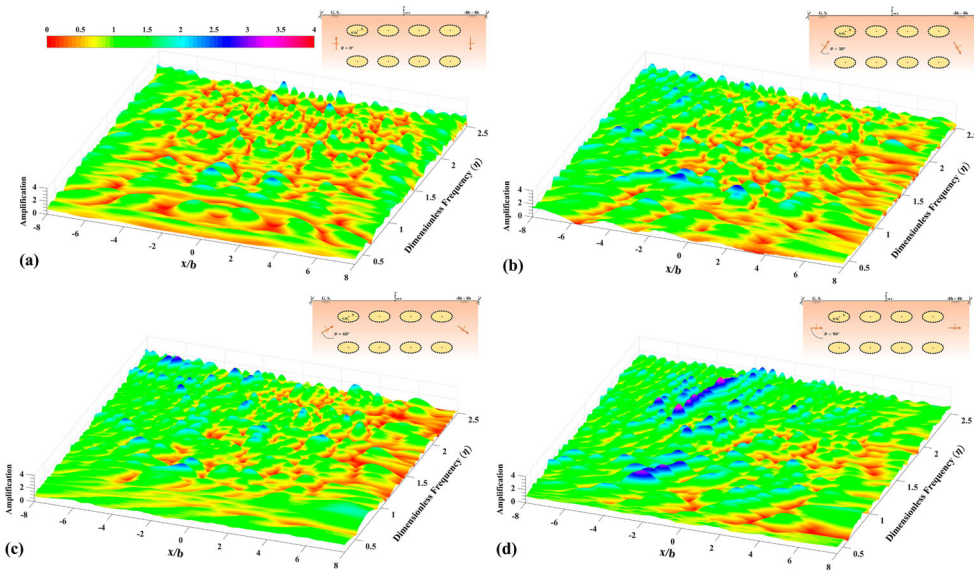

Figure 18. The 3D amplification of the ground surface versus different dimensionless frequencies for the model of eight elliptical inclusions subjected to the *SH*-waves and the incident angle of (a) $\theta = 0°$, (b) $\theta = 30°$, (c) $\theta = 60°$, and (d) $\theta = 90°$.
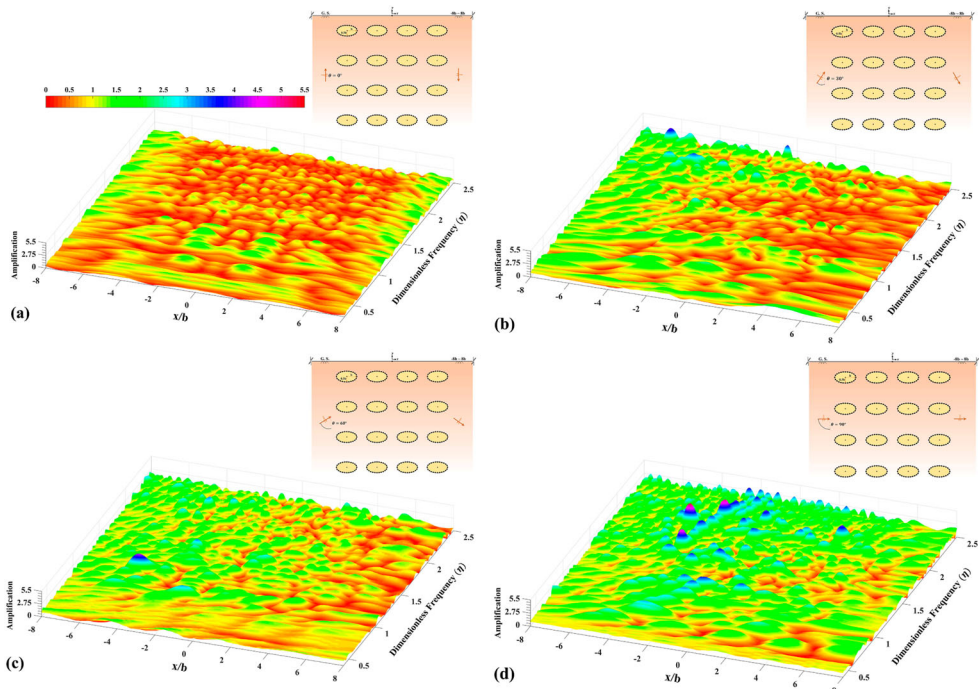
Figure 19. The 3D amplification of the ground surface versus different dimensionless frequencies for the model of 16 elliptical inclusions subjected to the *SH*-waves and the incident angle of (a) $\theta = 0°$, (b) $\theta = 30°$, (c) $\theta = 60°$, and (d) $\theta = 90°$.

the surface. The main volume of the refraction phase is trapped inside the inclusions and experience intermittent reflections. This effect can significantly increase the amplification on the surface. Moreover, because of the rotary shape of inclusions, the incident waves can crawl on the boundary of inclusions and reach the surface as well. The reflected and crawler waves helped the trapped waves to increase the values of amplification at a certain distance to the inclusions. Therefore, in some specific frequencies, one can see the amplifications equal to 2.5 between the location of inclusions. In Figure 12(b), the inclination of the wave-front to $\theta = 30°$ destroyed the symmetry of response such that extremely low amplifications are observed behind the location of inclusions relative to the angle of the wave-front. However, the maximum amplification of about 2.7 is obtained in the side of waves' entrance. When the incidence angle is $\theta = 60°$ (Figure 12(c)), the maximum amplifications occur where the incident waves are collided directly to the inclusions and then reflected reversely. Then, the reflected waves encounter the ground surface and increase the amplifications to about 2.5, which is slightly lower than the case of $\theta = 30°$, because of the more intense increase in the blocking effect of inclusions. However, still can see some amplified locations on the other side of inclusions, which emerged due to the trapped waves. In the model of twin circular inclusions with the angle of $\theta = 90°$ (Figure 12(d)), a high amplification is seen in the location of first inclusion. In this case, the main reason for amplifications to about 3 is the simplicity of the reflected waves to reach the surface due to the barrier effect of inclusions in front of the transient waves. In addition, because of the circular shape of inclusions, the crawler waves creep horizontally on the boundaries and their

effect on the amplification appears on the behind side of inclusions. When the inclusions are regularly distributed in two rows (Figure 13), the transient waves are mainly reflected or absorbed directly by the inclusions of lower-level; thus, reduction of the impact waves to
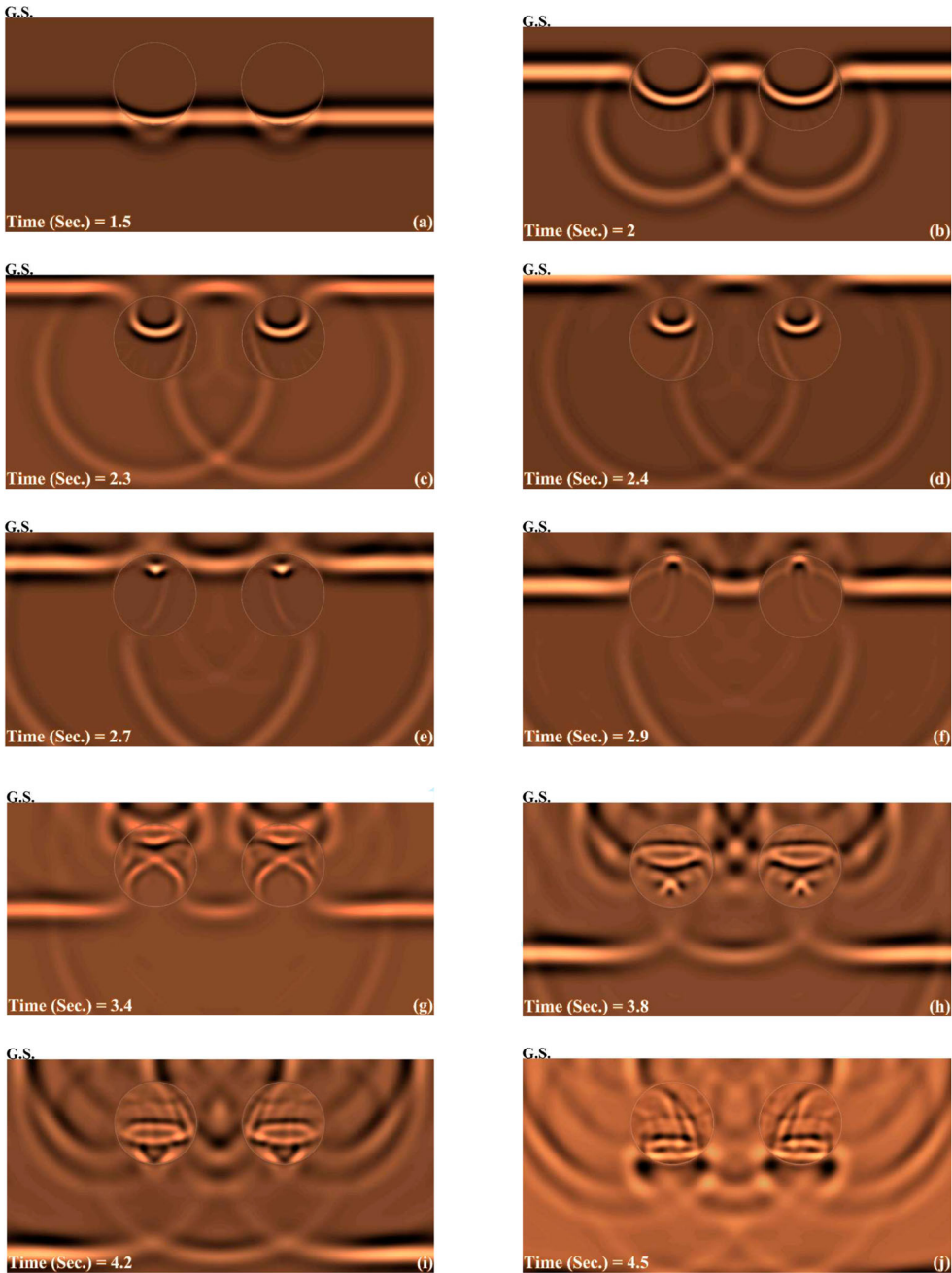

Figure 20. Wave propagation snapshots and the procedure of the *SH*-waves dispersion below the surface, for the model of twin circular inclusions for incident angle of $\theta = 0°$.

the upper inclusions leads to decreasing the volume of trapped waves near to the surface and lower amplification. In the following, the frequency-domain results of 8 and 16 circular inclusions are presented. The obtained responses show that the highest amplification is
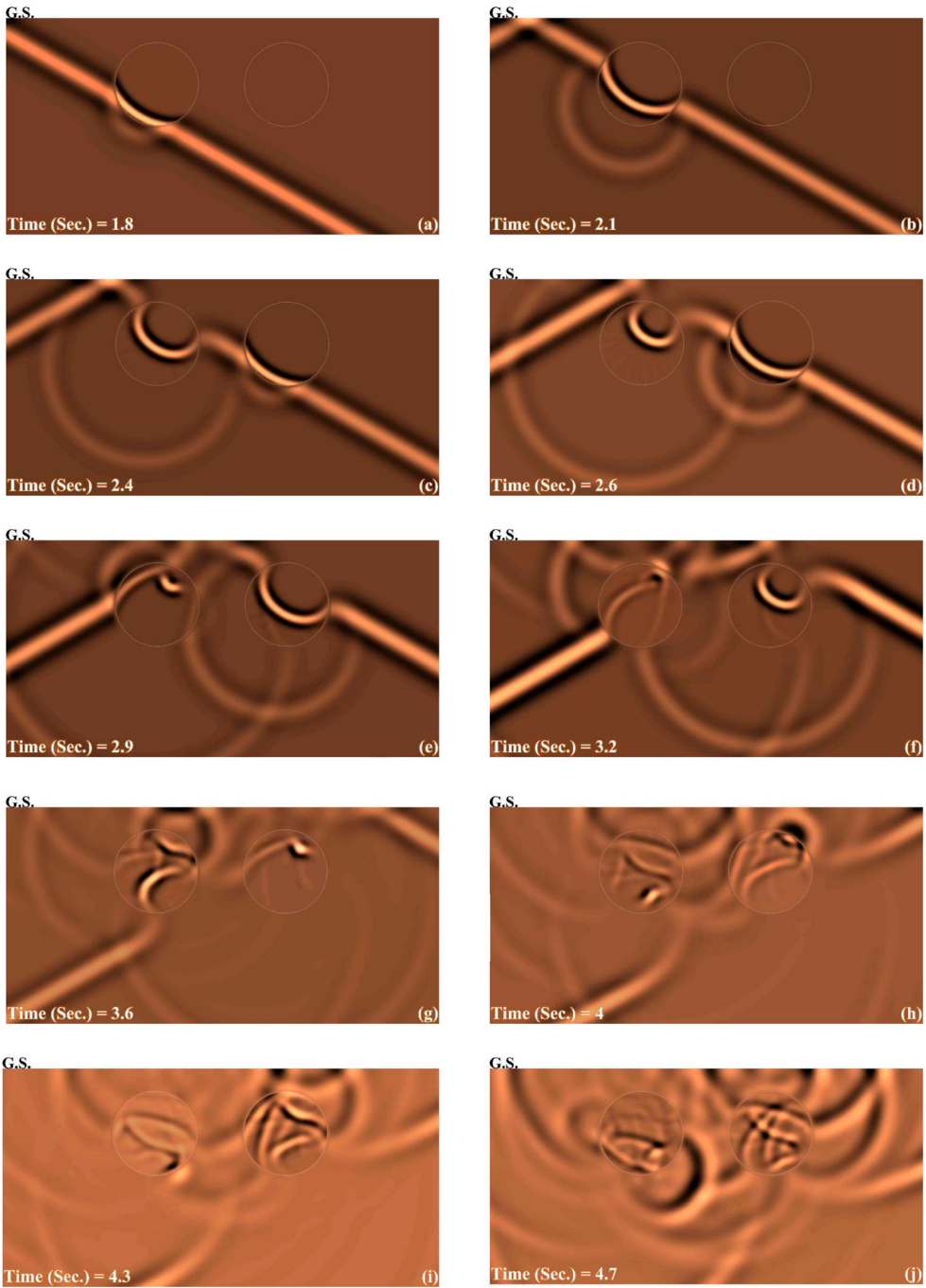

Figure 21. Wave propagation snapshots and the procedure of the *SH*-waves dispersion below the surface, for the model of twin circular inclusions for incident angle of $\theta = 30°$.

achieved when the incident waves are applied horizontally. Moreover, increasing the number of rows has increased the maximum amplification, which is clearly visible in Figures 14 and 15(d).
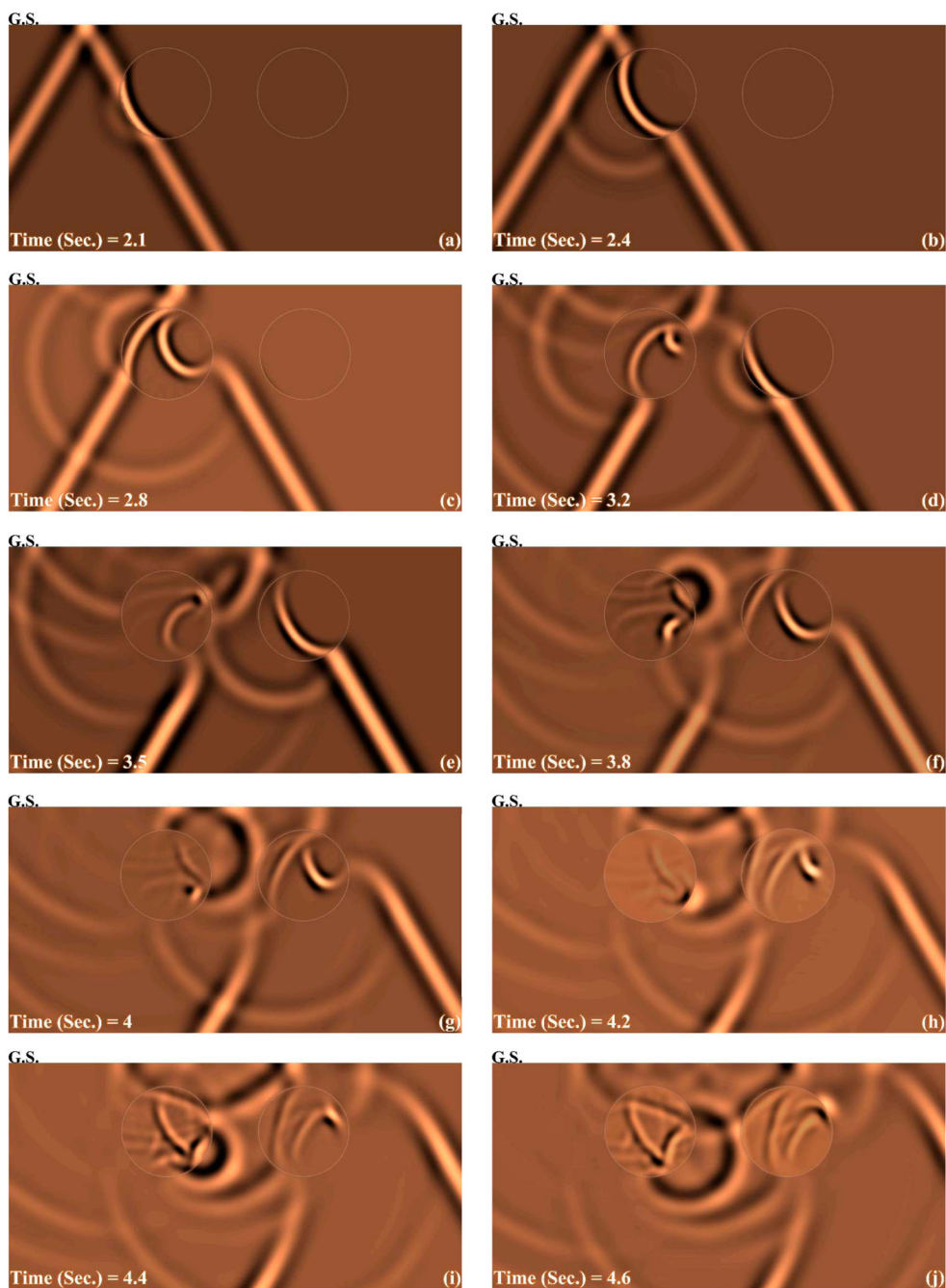

Figure 22. Wave propagation snapshots and the procedure of the *SH*-waves dispersion below the surface, for the model of twin circular inclusions for incident angle of $\theta = 60°$.

The 3D amplification patterns of multiple elliptical inclusions are presented in Figures 16–19. Comparing the response of twin elliptical inclusions subjected to vertical incident waves (Figure 16(a)) with a similar circular model (Figure 12(a)) shows that when the inclusions are elliptical, the maximum amplifications are concentrated on the locations of the
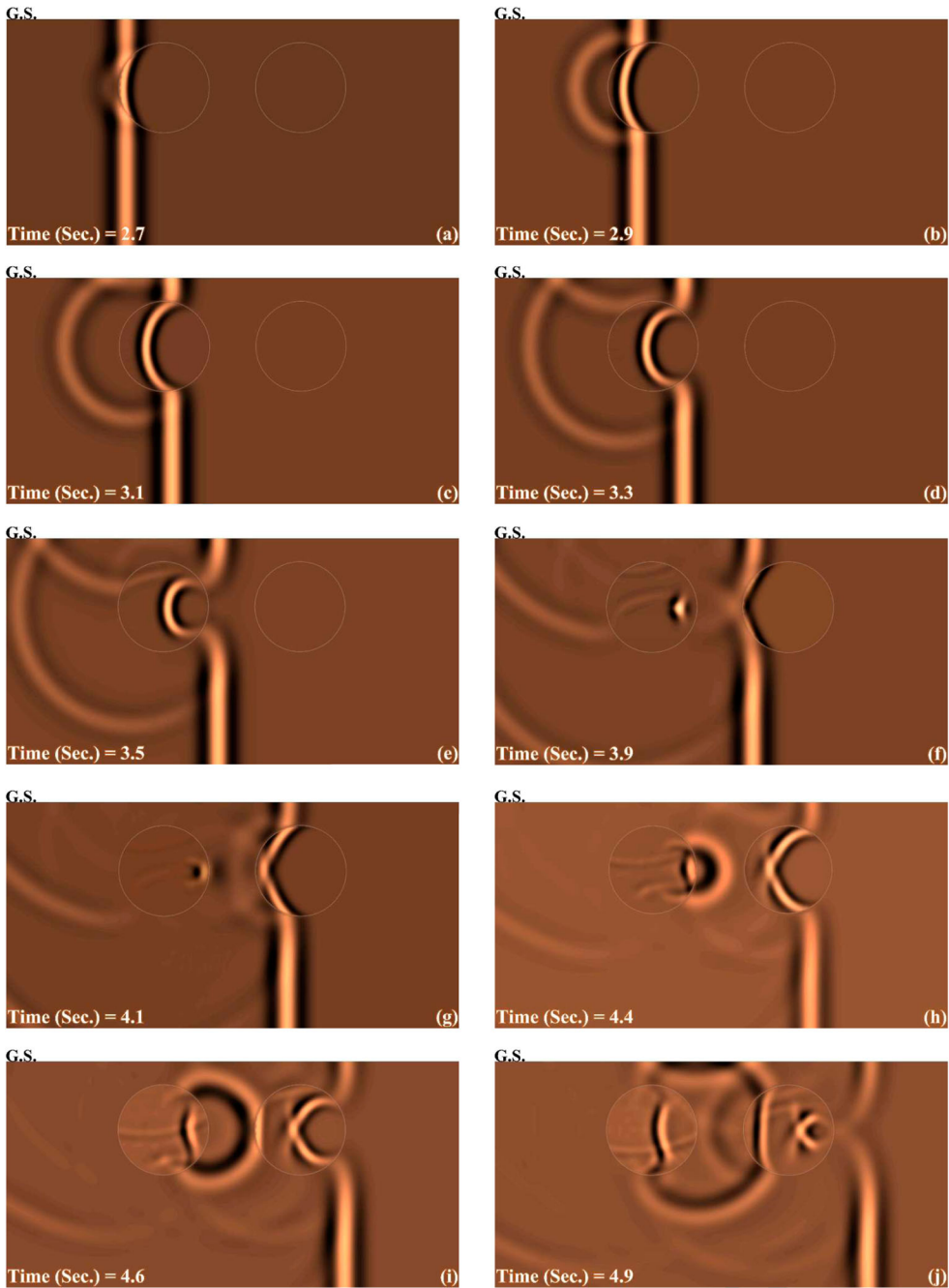

Figure 23. Wave propagation snapshots and the procedure of the *SH*-waves dispersion below the surface, for the model of twin circular inclusions for incident angle of $\theta = 90°$.

surface where the inclusions are placed. However, in the model of circular inclusions, the amplified points emerge between the inclusions. The main differences in amplifications are because of the specific shape of elliptical inclusions. These inclusions transversely reflect the
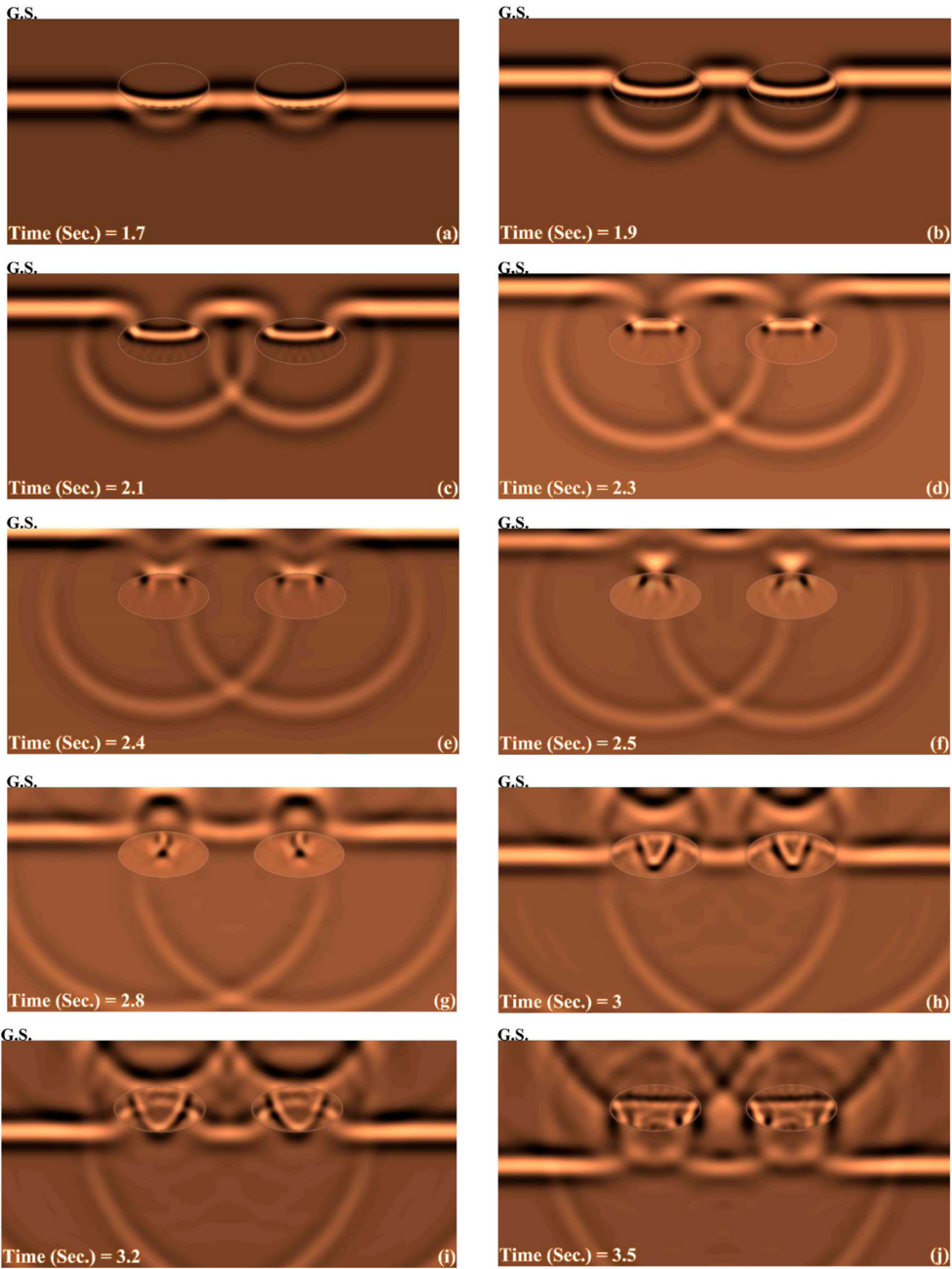

Figure 24. Wave propagation snapshots and the procedure of the *SH*-waves dispersion below the surface, for the model of twin elliptical inclusions for incident angle of $\theta = 0°$.

collided waves from the lower boundaries of inclusions and prevent the creation of crawler phases of transient waves. The wide and smaller medium of elliptical inclusions helps absorption and trapping of the waves, leading to the concentration of the amplifications

Figure 25. Wave propagation snapshots and the procedure of the *SH*-waves dispersion below the surface, for the model of twin elliptical inclusions for incident angle of $\theta = 30°$.

Figure 26. Wave propagation snapshots and the procedure of the *SH*-waves dispersion below the surface, for the model of twin elliptical inclusions for incident angle of $\theta = 60°$.

right above the location of inclusions. By inclination of the waves front to $\theta = 30°$ (Figure 16(b)), the maximum amplification of 2.4 is obtained, which is lower than the similar circular case (Figure 12(b)). In this model, the barrier effect of inclusions became stronger than the
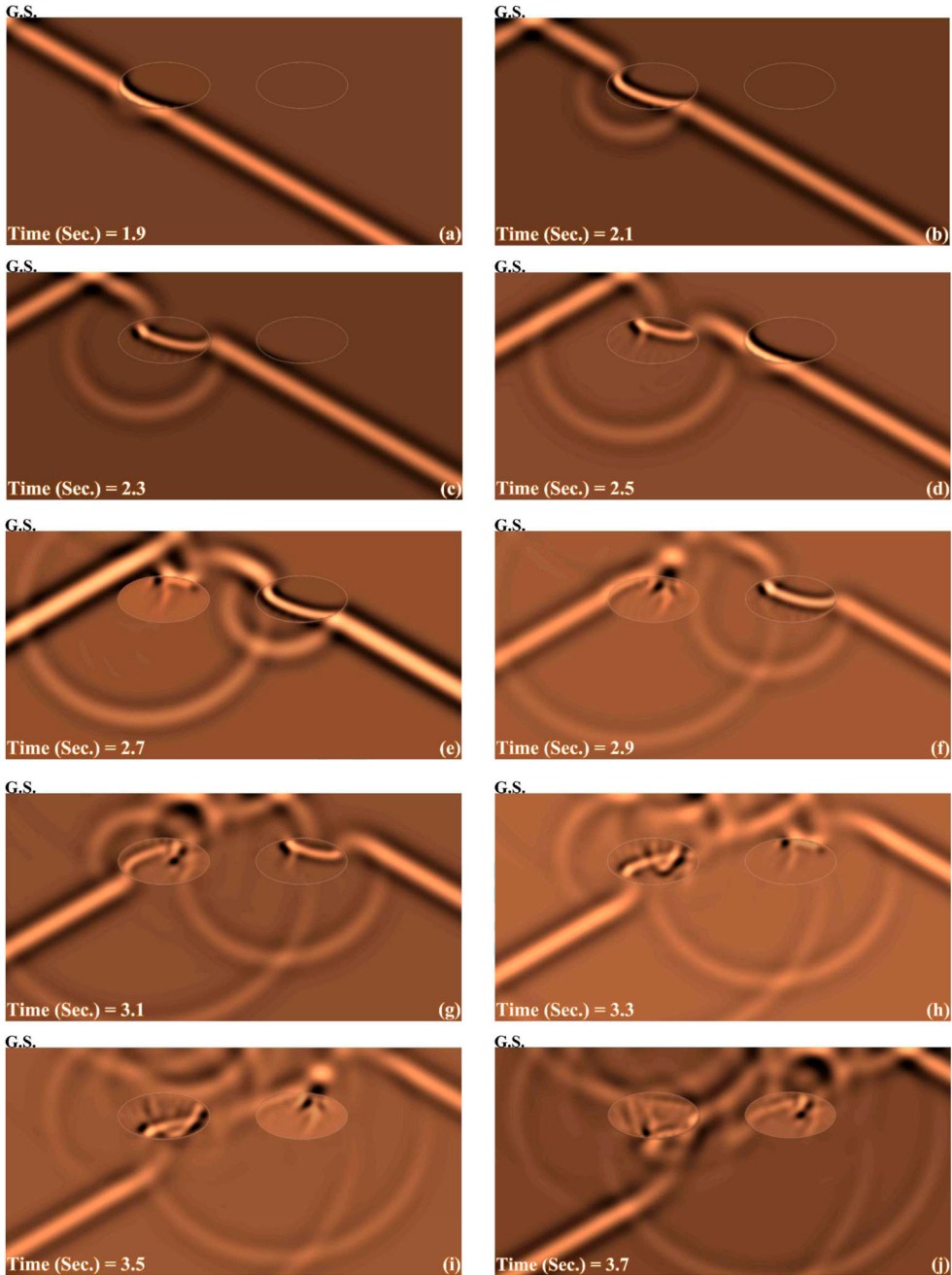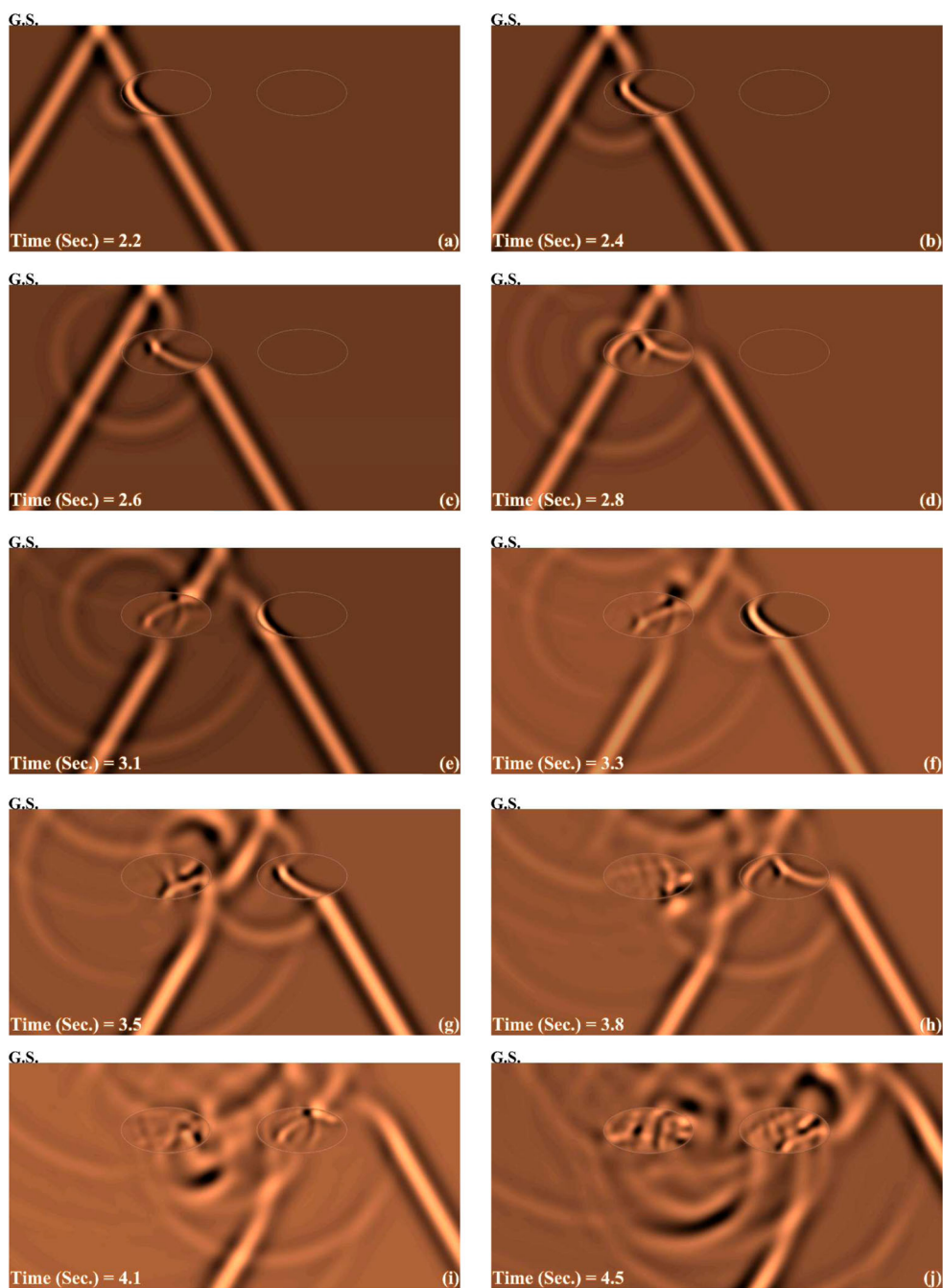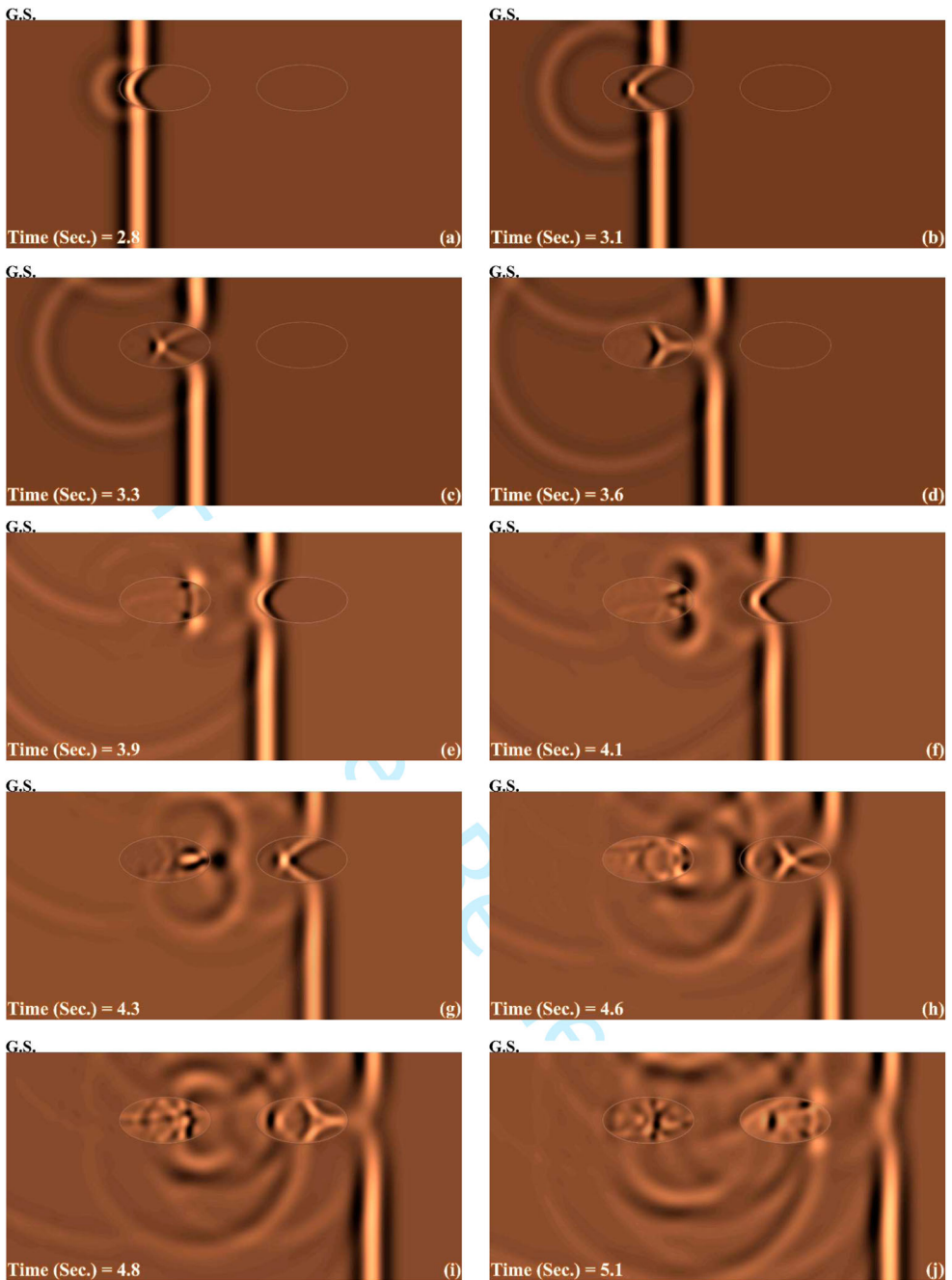
Figure 27. Wave propagation snapshots and the procedure of the *SH*-waves dispersion below the surface, for the model of twin elliptical inclusions for incident angle of $\theta = 90°$.

circular model. As a result, it increased the intensity of the shadow zone behind the inclusions and decreased the maximum values of amplification because of the lower volume of trapped waves. When the incident waves are applied by $\theta = 60°$ (Figure 16(c)), the weak

role of elliptical inclusions in preventing the wave passage is significant and the crawler waves are simply creeped along the boundaries. This effect is sharper when the wave-front reached the horizon (Figure 16(d)). Although the maximum amplification of about 3.4 is achieved in Figure 16(d), the amplified zones are very small and the amplifications occur in the collision point of direct incident waves to the first inclusion. As the responses show in Figure 17, increasing the number of rows can decrease the amplifications of the surface. Furthermore, increasing the number of inclusions leads to the growth of amplification due to the harder exit of the trapped waves. In the following, the responses of 8 and 16 elliptical inclusions are presented.

7.4. Wave propagation snapshots

Wave propagation below the surface is illustrated using wave scattering snapshots at different times. Figures 20–27 show the diffraction of *SH*-waves in the presence of twin circular/elliptical models for the incident angles of 0°, 30°, 60°, and 90°. To preparation of the snapshots, 14028 and 10201 internal points are considered into the main domain and each of inclusions, respectively. The surface range of $-5b$ to $5b$ and the depth of $-5b$ were considered in all snapshots. The results indicate the reflected and crawler phases of seismic waves on the boundary of inclusions. Moreover, they show the effect of trapped waves inside the medium of inclusions and between their boundaries and ground surface, which become even sharper over time.

8. Conclusion

A numerical direct TD-BEM based on half-space Green's functions was implemented in developing the algorithm of DASBEM to prepare the model of a half-plane cluttered with arbitrarily shaped multiple subsurface inclusions, subjected to scattering obliquely incident plane *SH*-waves. To establish the model, the discretization was concentrated only around the interfaces of inclusions connected to the surrounding domain. Utilizing the sub-structuring process, the problem was decomposed into a multi-pitted half-plane and a system of closed alluvial solids. By applying the method to the separated parts of the model and obtaining all matrices, the coupled matrix can be determined through satisfying continuity conditions on the interfaces. After solving the final equation in the time-domain, the boundary values including displacements/tractions were obtained. The accuracy of the method was examined by analyzing several examples. Comparing the responses with those presented in the previously published works revealed a good agreement and high accuracy of the proposed method. To complete the results, the synthetic seismograms of the surface were illustrated in the presence of multiple subsurface circular/elliptical inclusions. Then, by converting the time-domain responses to frequency-domain, the amplification patterns and displacements of the ground surface were depicted. Finally, to demonstrate the wave's propagation below the surface, the wave scattering snapshots were presented at different times. The main results of the present paper can be summarized as follows:

    (1) The half-plane TD-BEM was able to prepare the simple models for time-history step-by-step seismic analysis of the ground surface in the presence of arbitrarily shaped multiple subsurface inclusions.

(2) Synthetic seismograms of the surface showed that the amplitudes were reduced behind the location of inclusions relative to the direction of the wave-front. The inclusions were dispersed in the surface and absorbed the most part of incoming waves. Moreover, increasing the number of inclusions has a direct impact on holding seismic waves in the medium, which is the main reason for more intensity of displacements on the surface.

(3) By comparing the seismic responses of multiple underground cavities [61] and the present results, it was observed that the role of subsurface inclusions was weaker on the seismic isolation to create the safe area on the ground surface. Because of the intermittent reflections of the absorbed waves trapped inside the inclusions or between their boundaries and ground surface, the duration of convergence time and value of amplification on the surface increased.

(4) In circular-shaped inclusions, the incidence waves easily crept on the boundaries because of the rotary section of inclusions and the amplitude of crawler waves is higher than the reflected waves. When the inclusions are elliptical, the specific shape of elliptical inclusions diminishes the amplitude of crawler waves and the trapped waves. However, more iterative reflections of trapped waves occurred.

(5) The distribution of the inclusions in regular rows decreased the impact of incidence waves on the surface. When the incidence angle was vertical, the largest portion of waves is reflected and trapped immediately by the inclusions embedded in the lower rows, leading to a decreased contribution of inclusions in the first row and the vibration of diagrams. By applying the incident waves horizontally, the first column of inclusions blocked the paths of the seismic waves and the highest amplitudes were formed at the first collision side.

(6) By increasing the inclusion rows, the amplifications were decreased on the surface. In addition, increasing the number of inclusions led to the growth of amplification due to the harder exit of the trapped waves.

The proposed method can be utilized by geotechnical/mechanical engineers for transient analysis of multiple heterogeneous topographical features and composite materials in the field of earthquake engineering. Moreover, this method is practically recommended to researchers working on the time-history analysis of such materials with arbitrarily shaped multi-inhomogeneity.

Disclosure statement

No potential conflict of interest was reported by the authors.

ORCID

Saeed Mojtabazadeh-Hasanlouei http://orcid.org/0000-0001-8508-4837
Mehdi Panji http://orcid.org/0000-0002-3240-7775
Mohsen Kamalian http://orcid.org/0000-0001-5523-3520

References

[1] Sánchez-Sesma FJ, Palencia VJ, Luzón F. Estimation of local site effects during earthquakes: an overview. ISET J Earthq Tech. 2002;39(3):167–193.

[2] Simons DA. Scattering of *SH*-waves by thin, semi-infinite inclusions. Int J Sol Struct. 1979;16:177–192.

[3] Kikuchi M. Dispersion and attenuation of elastic waves due to multiple scattering from inclusions. Phys Earth Planet Inter. 1981a;25:159–162.

[4] Kikuchi M. Dispersion and attenuation of elastic waves due to multiple scattering from cracks. Phys Earth Planet Inter. 1981b;27:100–105.

[5] Coussy O. Scattering of elastic waves by an inclusion with an interface crack. Wave Motion. 1984;6:223–236.

[6] Wang YS, Wang D. Scattering of elastic waves by a rigid cylindrical inclusion partially deboned from its surrounding matrix-I. Int J Sol Struct. 1996;33(19):2789–2815.

[7] Zhao JX, Qi H. Scattering of plane *SH*-wave from a partially deboned shallow cylindrical elastic inclusion. J Mech. 2009;25(4):411–419.

[8] Conoir JM, Norris AN. Effective wavenumbers and reflection coefficients for an elastic medium containing random configurations of cylindrical scatterers. Wave Motion. 2010;47:183–197.

[9] Lee WM, Chen JT. Scattering of flexural wave in a thin plate with multiple circular inclusions by using the multipole method. Int J Mech Sci. 2011;53(8):617–627.

[10] Qi H, Yang R, Guo J, et al. Dynamic responses of a plate with multiple inclusions and depressions subjected to *SH*-waves. Mech Adv Mat Struct. 2020. DOI:10.1080/15376494.2020.1801915.

[11] Manoogian ME, Lee VW. Diffraction of *SH*-waves by subsurface inclusion of arbitrary shape. J Eng Mech. 1996;122(2):123–129.

[12] Lysmer J, Drake LA. A finite element method for seismology. Meth Comp Phys. 1972;11:181–216.

[13] Smith WD. The application of finite element analysis to body wave propagation problems. Geophys J Royal Astronom Soc. 1975;42(2):747–768.

[14] Day SM. (1977). Finite element analysis of seismic scattering problems [Dissertation]. University of California, San Diego.

[15] Kawase H, Sato T. Simulation analysis of strong motions in the Ashigara valley considering one- and two-dimensional geological structures. J Phys Earth. 1992;40:27–56.

[16] Zhang J, Katsube N. A hybrid finite element method for heterogeneous materials with randomly dispersed elastic inclusions. FE Analy Desig. 1995;19:45–55.

[17] Nakasone Y, Nishiyama H, Nojiri T. Numerical equivalent inclusion method: a new computational method for analyzing stress fields in and around inclusions of various shapes. Mat Sci Eng. 2000;285(1-2):229–238.

[18] Boore DM. A note on the effect of simple topography on seismic *SH*-waves. Bull Seism Soc Am. 1972;62:275–284.

[19] Ohtsuki A, Harumi K. Effects of topography and subsurface inhomogeneities on seismic *SV*-waves. Earthq Eng Struct Dyn. 1983;11:441–462.

[20] Moczo P, Bard PY. Wave diffraction, amplification and differential motion near strong lateral discontinuities. Bull Seism Soc Am. 1993;83:85–106.

[21] Dominguez J, Meise T. On the use of the BEM for wave propagation in infinite domains. Eng Analy BE. 1991;8(3):132–138.

[22] Panji M, Kamalian M, Asgari-Marnani J, et al. Transient analysis of wave propagation problems by half-plane BEM. Geophys J Int. 2013;194:1849–1865.

[23] Ahmad S, Banerjee PK. Multi-domain BEM for two-dimensional problems of elastodynamics. Int J Numer Meth Eng. 1988;26(4):891–911.

[24] Panji M, Asgari-Marnani J, Tavousi-Tafreshi S. Evaluation of effective parameters on the underground tunnel stability using BEM. J Struct Eng and Geotech. 2011;1(2):29–37.

[25] Panji M, Koohsari H, Adampira M, et al. Stability analysis of shallow tunnels subjected to eccentric loads by a boundary element method. J Rock Mech and Geotech Eng. 2016a;8(4):480–488.

[26] Hadley PK. (1987). Scattering of waves by inclusions in a nonhomogeneous elastic half-space solved by boundary element method [Dissertation]. Princeton University, Princeton.

[27] Kamalian M, Jafari MK, Sohrabi-Bidar A, et al. Time-domain two-dimensional site response analysis of non-homogeneous topographic structures by a hybrid FE/BE method. Soil Dyn Earthq Eng. 2006;26(8):753–765.

[28] Parvanova SL, Dineva PS, Manolis GD, et al. Dynamic response of a solid with multiple inclusions under anti-plane strain conditions by the BEM. Comp Struct. 2014;139:65–83.

[29] Parvanova SL, Manolis GD, Dineva PS. Wave scattering by nano-heterogeneities embedded in an elastic matrix via BEM. Eng Analy with BE. 2015a;56:57–69.

[30] Parvanova SL, Vasilev GP, Dineva PS, et al. Dynamic analysis of nano-heterogeneities in a finite-sized solid by boundary and finite element methods. Int J Sol Struct. 2015b;80:1–18.

[31] Panji M, Ansari B, Asgari-Marnani J. Stress analysis of shallow tunnels in the multi-layered soils using half-plane BEM [In Persian]. J Transp Infrast Eng. 2016b;2(1):17–32.

[32] Panji M, Ansari B. Modeling pressure pipe embedded in two-layer soil by a half-plane BEM. Comp Geotech. 2017a;81(C):360–367.

[33] Dong CY, Lo SH, Cheung YK. Numerical solution for elastic half-plane inclusion problems by different integral equation approaches. Eng Analy BE. 2004;28:123–130.

[34] Dravinski M. Ground motion amplification due to elastic inclusion in a half-space. Earthq Eng Struct Dyn. 1983;11:313–335.

[35] Niwa Y, Hirose S. Application of the boundary integral equation (BIE) method to transient response analysis of inclusions in half space. Wave Motion. 1986;8:77–91.

[36] Hadley PK, Askar A, Cakmak AS. (1989). Scattering of waves by inclusions in a nonhomogeneous elastic half space solved by boundary element methods. Technical Report: NCEER-89-0027.

[37] Benites R, Aki K, Yomigida K. Multiple scattering of SH-waves in 2-D media with many cavities. Pure Appl Geophys. 1992;138:353–390.

[38] Benites R, Roberts PM, Yomogida K, et al. Scattering of elastic waves in 2-D composite media I. theory and test. Phys Earth Planet Int. 1997;104:161–173.

[39] Yomogida K, Benites R, Roberts PM, et al. Scattering of elastic waves in 2-D composite media II. Waveforms and spectra. Phys Earth Planet Inter. 1997;104:175–192.

[40] Yao Z, Kong F, Wang H, et al. 2D Simulation of composite materials using BEM. Eng Analy BE. 2004;28:927–935.

[41] Rus G, Gallego R. Boundary integral equation for inclusion and cavity shape sensitivity in harmonic elastodynamics. Eng Analy BE. 2005;29:77–91.

[42] Mogilevskaya S, Crouch S, Stolarski H. Multiple interacting circular nano-inhomogeneities with surface/interface effects. J Mech Phys Solids. 2008;56:2298–2327.

[43] Chen K, Chen JT, Kao J. Regularized meshless method for antiplane shear problems with multiple inclusions. Int J Numer Meth Eng. 2008;73(9):1251–1273.

[44] Yu CW, Dravinski M. Scattering of plane harmonic *SH*-wave by a completely embedded corrugated scatterer. Int J Numer Meth Eng. 2009;78:196–214.

[45] Yu CW, Dravinski M. Scattering of plane harmonic *P*, *SV* and *Rayleigh*-waves by a completely embedded corrugated elastic inclusion. Wave Motion. 2010;47:156–167.

[46] Parvanova SL, Dineva PS, Manolis GD. Dynamic behavior of a finite-sized elastic solid with multiple cavities and inclusions using BIEM. Acta Mech. 2013;224:597–618.

[47] Dravinski M, Sheikhhassani R. Scattering of a plane harmonic *SH*-wave by a rough multilayered inclusion of arbitrary shape. Wave Motion. 2013;50:836–851.

[48] Peters F, Barra LP. An inverse geometric problem: position and shape identification of inclusions in a conductor domain. Eng Analy BE. 2013;37:1392–1400.

[49] Lee Y, Chen JT. Null-field approach for the antiplane problem with elliptical holes and/or inclusions. Compos Part B: Eng. 2013;44(1):283–294.

[50] Chen JT, Kao SK, Hsu YH, et al. Scattering problems of the *SH*-wave by using the null-field boundary integral equation method. J Earthq Eng. 2017;22(5):1–35.

[51] Sheikhhassani R, Dravinski M. Scattering of a plane harmonic *SH*-wave by multiple layered inclusions. Wave Motion. 2014;51(3):517–532.

[52] Sheikhhassani R, Dravinski M. Dynamic stress concentration for multiple multilayered inclusions embedded in an elastic half-space subjected to *SH*-waves. Wave Motion. 2016;62:20–40.

[53] Ba Z, Yin X. Wave scattering of complex local site in a layered half-space by using a multidomain IBEM: incident plane *SH*-waves. Geophys J Int. 2016;205(3):1382–1405.

[54] Jobin TM, Ramji M, Khaderi SN. Numerical evaluation of the interaction of rigid line inclusions using strain intensity factors. Int J Mech Sci. 2019;153-154:10–20.

[55] Feng YD, Wang YS, Zhang ZM. Transient scattering of *SH*-waves from an inclusion with a unilateral frictional interface, a 2D time domain boundary element analysis. Comm Numer Meth Eng. 2003;19:25–36.

[56] Kamalian M, Gatmiri B, Sohrabi-Bidar A. On time-domain two-dimensional site response analysis of topographic structures by BEM. J Seism Earthq Eng. 2003;5(2):35–45.

[57] Mykhaskiv V. Transient response of a plane rigid inclusion to an incident wave in an elastic solid. Wave Motion. 2005;41:133–144.

[58] Huang Y, Crouch SL, Mogilevskaya SG. A time domain direct boundary integral method for a viscoelastic plane with circular holes and elastic inclusions. Eng Analy BE. 2005;29:725–737.

[59] Lei J, Wang YS, Huang Y, et al. Dynamic crack propagation in matrix involving inclusions by a time-domain BEM. Eng Analy BE. 2012;36(5):651–657.

[60] Panji M, Ansari B. Transient *SH*-wave scattering by the lined tunnels embedded in an elastic half-plane. Eng Analy BE. 2017b;84:220–230.

[61] Panji M, Mojtabazadeh-Hasanlouei S. Time-history responses on the surface by regularly distributed enormous embedded cavities: incident *SH*-waves. Earthq Sci. 2018;31:1–17.

[62] Panji M, Mojtabazadeh-Hasanlouei S. Seismic amplification pattern of the ground surface in presence of twin unlined circular tunnels subjected to *SH*-waves [In Persian]. J Transp Infrast Eng. 2019. DOI:10.22075/jtie.2019.16056.1342

[63] Huang L, Liu Z, Wu C, et al. The scattering of plane *P*, *SV* waves by twin lining tunnels with imperfect interfaces embedded in an elastic half-space. Tunn Underg Space Tech. 2019;85:319–330.

[64] Panji M, Mojtabazadeh-Hasanlouei S, Yasemi F. A half-plane time-domain BEM for *SH*-wave scattering by a subsurface inclusion. Comp Geosci. 2020;134; DOI:10.1016/j.cageo.2019.104342.

[65] Panji M, Mojtabazadeh-Hasanlouei S. Transient response of irregular surface by periodically distributed semi-sine shaped valleys: incident *SH*-waves. J Earthq Tsu. 2020. DOI:10.1142/S1793431120500050

[66] Ricker N. The form and laws of propagation of seismic wavelet. Geophys. 1953;18(1):10–40.

[67] Reinoso E, Wrobel LC, Power H. Preliminary results of the modeling of the Mexico City valley with a two-dimensional boundary element method for the scattering of *SH*-waves. Soil Dyn Earthq Eng. 1993;12(8):457–468.

[68] Brebbia CA, Dominguez J. Boundary elements, an introductory course. Boston: Comp Mech Pub; 1989.

[69] Dominguez J. Boundary elements in dynamics. Boston: Comp Mech Pub; 1993.

[70] Kawase H. Time-domain response of a semi-circular canyon for incident *SV*, *P* and Rayleigh-waves calculated by the discrete wave-number boundary element method. Bull Seism Soc Am. 1988;78(4):1415–1437.

[71] MATLAB. The language of technical computing. V. 9.7. (R2019b). Natick: The MathWorks Inc; 2019.

[72] Dravinski M, Yu MC. Scattering of plane harmonic *SH*-waves by multiple inclusions. Geophys J Int. 2011;186:1331–1346.

[73] Keller JB. Geometrical theory of diffraction. J Opt Soc Am. 1962;52(2):116–130.

[74] Trifunac MD. Scattering of plane *SH*-waves by a semi cylindrical canyon. Earthq Eng Struct Dyn. 1973;3(1):267–281.